

## REPRODUCING KERNEL HIERARCHICAL PARTITION OF UNITY, PART II—APPLICATIONS

SHAOFAN LI AND WING KAM LIU\*

*Department of Mechanical Engineering, Northwestern University, 2145 Sheridan Road, Evanston, IL 60208, U.S.A.*

### SUMMARY

In this part of the work, the meshless hierarchical partition of unity proposed in [1], referred here as Part I, is used as a multiple scale basis in numerical computations to solve practical problems. The applications discussed in the present work fall into two categories: (1) a wavelet adaptivity refinement procedure; and (2) a so-called wavelet Petrov–Galerkin procedure.

In the applications of wavelet adaptivity, the hierarchical reproducing kernels are used as a multiple scale basis to compute the numerical solutions of the Helmholtz equation, a model equation of wave propagation problems, and to simulate shear band formation in an elasto-viscoplastic material, a problem dictated by the presence of the high gradient deformation. In both numerical experiments, numerical solutions with high resolution are obtained by inserting the wavelet-like basis into the primary interpolation function basis, a process that may be viewed as a spectral  $p$ -type refinement.

By using the interpolant that has synchronized convergence property as a weighting function, a wavelet Petrov–Galerkin procedure is proposed to stabilize computations of some pathological problems in numerical computations, such as advection–diffusion problems and Stokes’ flow problem; it offers an alternative procedure in stabilized methods and also provides some insight, or new interpretation of the method. Detailed analysis has been carried out on the stability and convergence of the wavelet Petrov–Galerkin method. Copyright © 1999 John Wiley & Sons, Ltd.

KEY WORDS: meshless methods; reproducing kernel particle method; partition of unity,  $p$ -adaptivity; wavelet Petrov–Galerkin method

### 1. INTRODUCTION

In [1], a meshless hierarchical interpolant basis is constructed, which has a distinct distribution of spectral contents of the interpolating object among the different bases; in other words, they

---

\* Correspondence to: Wing Kam Liu, Department of Mechanical Engineering, Northwestern University, 2145 Sheridan Road, Evanston, IL 60208, U.S.A. E-mail: w-liu@nwu.edu

Contract/grant sponsor: Office of Naval Research  
Contract/grant sponsor: Army Research Office  
Contract/grant sponsor: National Science Foundation  
Contract/grant sponsor: Tull Family Endowment Fund  
Contract/grant sponsor: Northwestern University  
Contract/grant sponsor: Army High Performance Computing Research Center; contract/grant numbers DAAH04-95-2-003/DAAH04-95-C-0008

consist a multi-spectral wave packet. As a matter of fact, as shown in Part I, the higher-order basis functions does fit into the definition of the pre-wavelet function.<sup>†</sup>

In this part of the work, the newly developed meshless hierarchical partition of unity is employed in numerical computations of several engineering problems, in order to test their actual performance and computational capability. Since the higher-order basis constitute a pseudo-spectral basis, it is natural to test them by solving the problems that are related to wave propagation, or acoustic problems, which extends the early work by Liu *et al.* [2, 3] and Uras *et al.* [4]. The first numerical example is to use the meshless hierarchical partition of unity to solve an one-dimensional Helmholtz equation, the Dirichlet-fixed bar problem. For this class of problems, the regular Galerkin/finite element methods have some deficiencies in capturing the high-frequency part of the solutions (see [5, 6], and references therein).

Our computation strategy in this case is very simple: by adding the wavelet shape functions into the primary interpolation basis to seek improvement of the numerical solutions. It is demonstrated numerically that by increasing the order of hierarchical basis, high-resolution solutions can be obtained in numerical computations. To extend the above numerical strategy to multiple-dimensional problems, in the second example, the meshless hierarchical partition of unity are employed in a computation to simulate the shear band formation in an elasto-viscoplastic material. In the computation, we add the wavelet-like basis into the primary shape function basis as a spectral  $p$ -type refinement desiring to capture high gradient deformation field in the solid. The improvement of numerical solutions has been observed in the computation. It is worth noting that unlike the conventional  $p$  finite element method, which blends the higher-order polynomial bubble modes into the primary shape function basis, the reproducing kernel hierarchical partition of unity adds wavelet modes into the original shape function basis; those wavelet bases are built-in through the original construction of the primary shape function basis, and they do not come from the additional higher-order polynomials, such as the  $h$ - $p$  clouds method proposed by Duarte and Oden [7] in the context of meshless setting. The main technical obstacle in the implementation of such a numerical strategy is the ill-conditioning of the resulting stiffness matrix and mass matrix, because adding a partition of nullity into a partition of unity will result in redundancy in the shape function basis. This very crucial issue is addressed in Section 3.

In addition to the wavelet refinement, the hierarchical partition of unity developed here can also form a so-called synchronized reproducing interpolant, which can be used as the weighting function in a Petrov–Galerkin stabilized procedure to deal with some pathological problems in numerical computations, such as advection–diffusion problem, Stokes’ flow problem, and others. Since the computation procedure is very similar to the widely spread Petrov–Galerkin stabilized method, we coin this particular procedure as the Wavelet–Petrov–Galerkin method with the belief that a general stabilized mechanism may exist for general wavelet functions.

## 2. NUMERICAL EXAMPLE I: HELMHOLTZ EQUATION

The Helmholtz equation, or reduced wave equation, presents many difficulties for conventional Galerkin/finite element procedures. An example of such difficulties is that the numerical solution does not preserve the ‘non-dispersive’ character of the exact solution [6, 8], which leads to both amplitude error as well as phase error. To overcome such difficulties, special techniques have to

---

<sup>†</sup>By ‘pre-wavelet’, we mean that the admissible conditions of the basic wavelet function is satisfied

be developed in dealing with Helmholtz equations, or hyperbolic systems in general. It has been found that ‘the higher-order  $p$ -element exhibit increased accuracy compared to low-order finite elements for the same order of degree of freedom’ ([5], p. 266).

Therefore, this is a very suitable testing problem that can examine the performance of the proposed meshless hierarchical partition of unity. Consider the following Dirichlet-fixed bar problem:

$$\frac{d^2u}{dx^2} + k^2u = F(x) \tag{1}$$

$$u(0) = \bar{u} \quad \text{and} \quad u(1) = 0 \tag{2}$$

$\forall u, v \in H^1([0, L])$ , the weak formulation is

$$\int_0^L \frac{du}{dx} \frac{dv}{dx} dx - \left. \frac{du}{dx} v \right|_0^L - k^2 \int_0^L uv dx + \int_0^L Fv dx = 0 \tag{3}$$

The numerical computation is performed on a uniform particle distribution over  $[0, L]$  with index set  $\Lambda = \{I \mid I = 1, 2, \dots, 11\}$ . We choose the fifth-order spline as a window function with a compact support radius  $R_I = a_I \varrho$ , where  $\varrho = \Delta x$ , and  $a_I$  is in a range 3.0–5.0, which implies that there are 5–9 nodes in the interior domain of the compact support. The generating polynomial basis is  $\mathbf{P} = (1, x, x^2, x^3)$ . Select a sub-index set  $\overset{\circ}{\Lambda} \subset \Lambda$ ,

$$\overset{\circ}{\Lambda} := \{I \in \Lambda, x_I \in (0, L)\}$$

and  $\text{card}\{\overset{\circ}{\Lambda}\} = 9$ ,  $\beta = 1, 2, 3$ . The multi-level hierarchical basis are displayed in Figure 1. Note that there is difference between hierarchical frame and the hierarchical basis. The reason that we called them as a hierarchical basis is because we eliminate the redundancy of the frame by taking out some of the higher-order wavelet shape functions at the end points,  $x = 0$  and  $x = L$ . One may compare Figure 1 with the corresponding hierarchical partition of unity, Figure 1 in Part I, and observe the subtle differences. It is not difficult to find that the hierarchical basis remains as a partition of unity inside the interior domain.

We solve the model equation by substituting the following hierarchical approximation into the weak formulation (3):

$$u_{[0]}^\rho(x) = \sum_{I \in \Lambda} u_I^{[0]} \Psi_I^{[0]}(x) \tag{4}$$

and

$$u_{[\beta]}^\rho(x) = \sum_{I \in \Lambda} u_I^{[0]} \Psi_I^{[0]}(x) + \sum_{I \in \overset{\circ}{\Lambda}} \sum_{\alpha=1}^{\beta} u_I^{[\alpha]} \Psi_I^{[\alpha]}(x), \quad \beta = 1, 2, 3 \tag{5}$$

where  $\{\Psi_I^{[0]}(x)\}$  is the basis of the zeroth-order kernel function, and  $\{\Psi_I^{[\alpha]}(x)\}$   $\alpha \neq 0$ , are the wavelet-like basis. In the following numerical calculations, the order  $\beta$  in equation (5) is kept on increasing, that is to add higher-order wavelet-like basis into the primary basis. The numerical solutions are carried out, and compared at four different wave numbers,  $k = 8, 16, 24, 32$ .

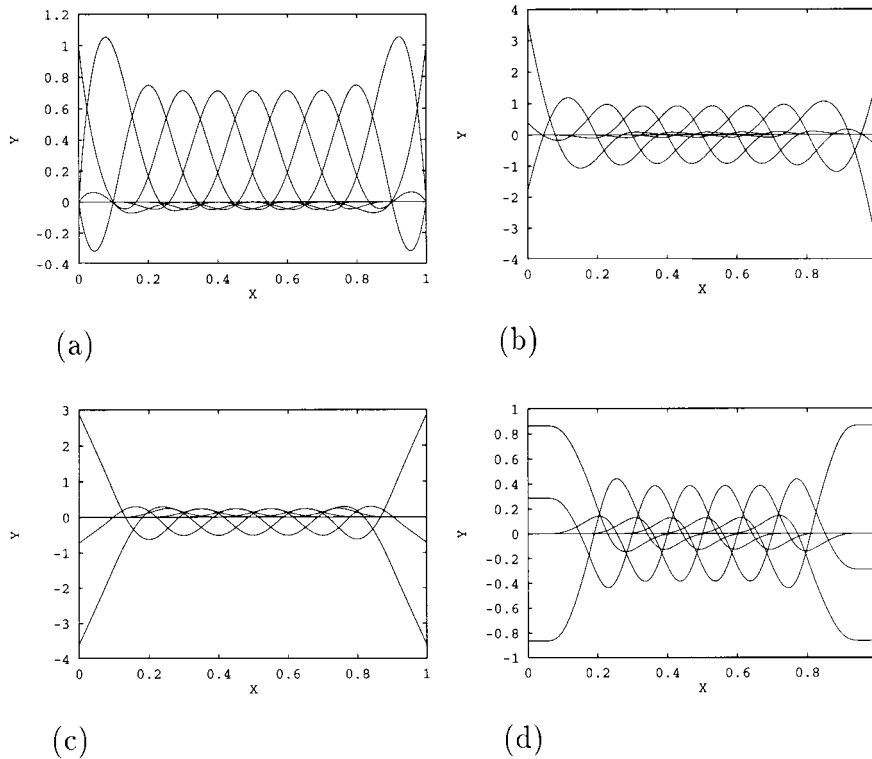


Figure 1. The hierarchical bases used in computation

For  $F(x)=0$ , the exact solution is

$$u(x) = \bar{u} \frac{\sin(k(L-x))}{\sin(kL)} \tag{6}$$

In Figures 2–5, the numerical solutions are plotted against the exact solution for four different wave numbers,  $k=8, 16, 24, 32$ . In all four examples, only 11 particles are used in the computation.

In Figure 2, one may find that in the case of 11-particle discretization the numerical solution  $u_{[0]}^o(x)$  is only accurate when wave number is below  $k=8$ , after that, both amplitude error and phase error occur. With the same discretization, we add the first-order wavelet basis into the primary shape function basis, and the numerical solution,  $u_{[1]}^o(x)$ , is accurate up to the wave number  $k=16$  (see Figure 3). By adding more wavelet-like bases into the primary shape function basis, not only the accuracy of the numerical solutions keep increasing, but also the range of such accurate solutions with respect to wave number is increasing as well. For  $\beta=2$ , which means that two wavelet bases have been added into the primary partition of unity, the accuracy range of the numerical solution,  $u_{[2]}^o(x)$ , is up to the wave number  $k=24$  (Figure 4). And the numerical solution,  $u_{[3]}^o(x)$ , is very close to exact solution at wave number  $k=32$  (Figure 5).

The same trend can be observed from the frequency responses of the numerical solutions. We plot the continuous frequency spectrum of numerical solutions at the middle point of the bar,

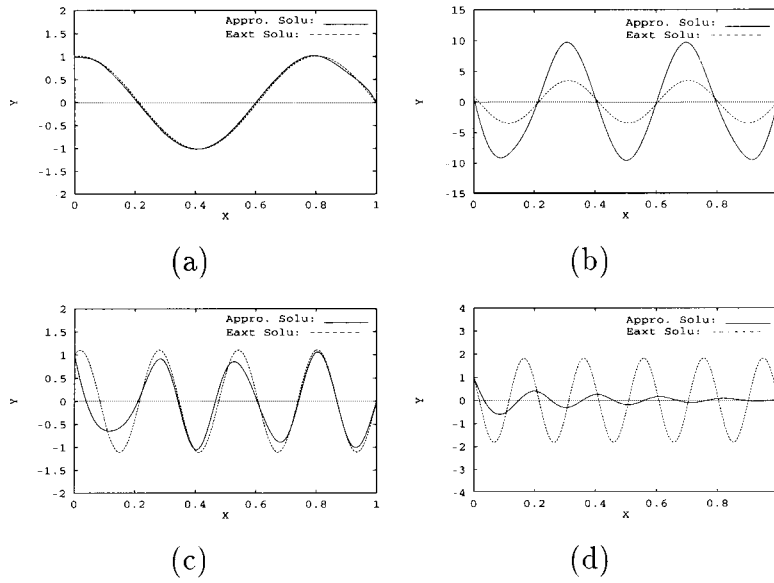


Figure 2. Dirichlet-fixed bar problem: Numerical solutions  $u_{[0]}^k(x)$  vs. the exact solution  $u(x)(\beta=0)$ : (a)  $k=8$ ; (b)  $k=16$ ; (c)  $k=24$ ; (d)  $k=32$

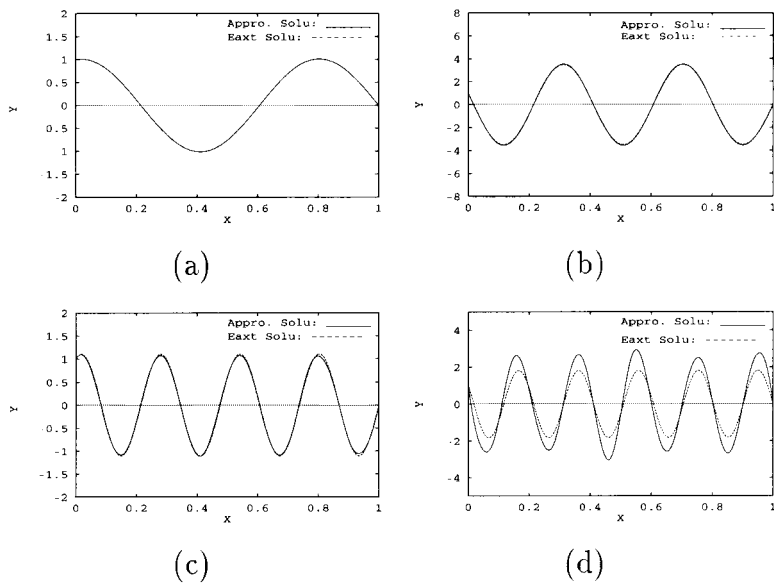


Figure 3. Dirichlet-fixed bar problem: numerical solutions  $u_{[1]}^k(x)$  vs. the exact solution  $u(x)(\beta=1)$ : (a)  $k=8$ ; (b)  $k=16$ ; (c)  $k=24$ ; (d)  $k=32$

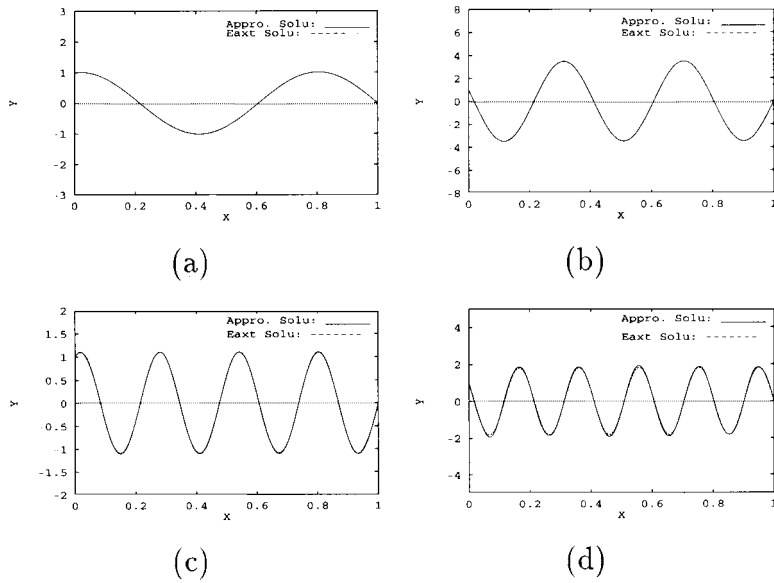


Figure 4. Dirichlet-fixed bar problem: numerical solutions  $u_{[2]}^{\theta}(x)$  vs. the exact solution  $u(x)$  ( $\beta=2$ ): (a)  $k=8$ ; (b)  $k=16$ ; (c)  $k=24$ ; (d)  $k=32$

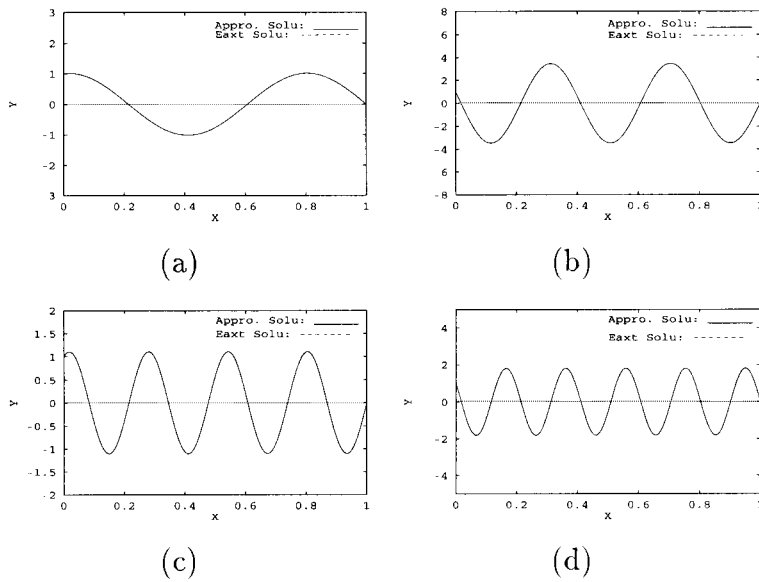


Figure 5. Dirichlet-fixed bar problem: numerical solutions  $u_{[3]}^{\theta}(x)$  vs. the exact solution  $u(x)$  ( $\beta=3$ ): (a)  $k=8$ ; (b)  $k=16$ ; (c)  $k=24$ ; (d)  $k=32$

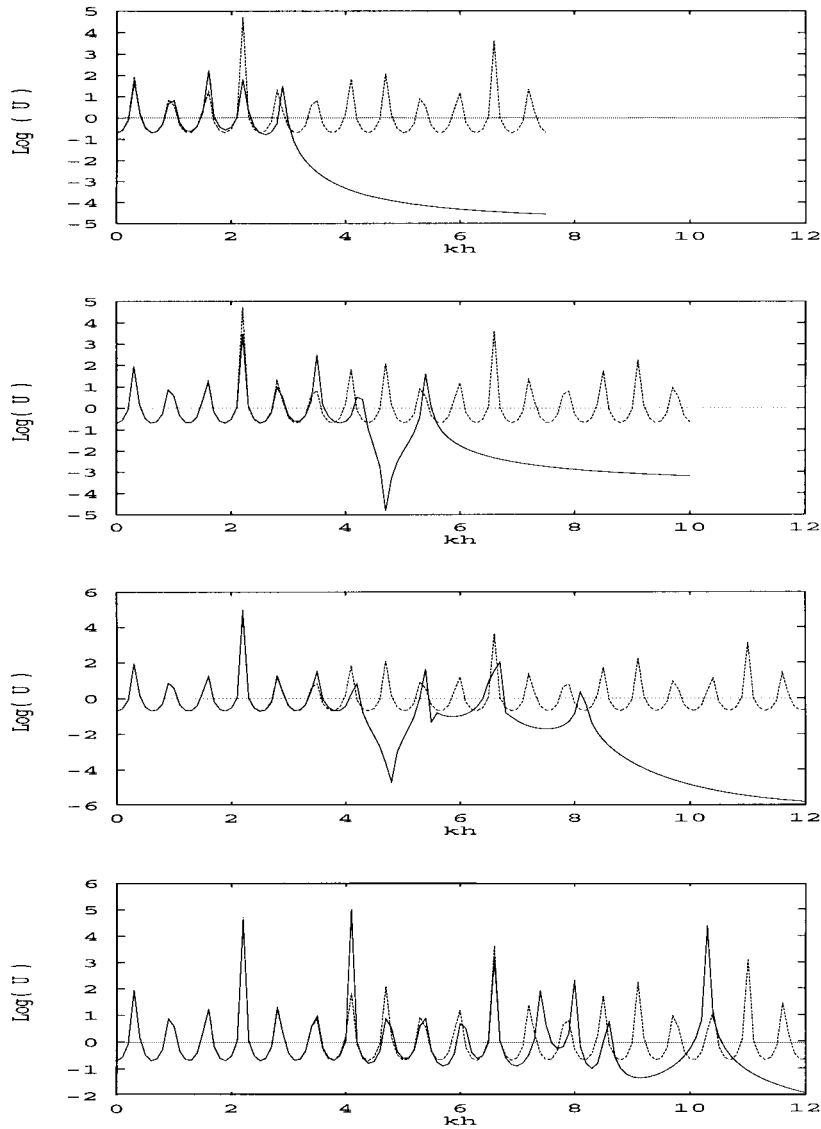


Figure 6. Frequency response: (a)  $\text{Log}(u_{[0]}^e(0.5, k))$ ; (b)  $\text{Log}(u_{[1]}^e(0.5, k))$ ; (c)  $\text{Log}(u_{[2]}^e(0.5, k))$ ; (d)  $\text{Log}(u_{[3]}^e(0.5, k))$ ; the dotted line: exact solution; the solid line: numerical solution

$x = 0.5$ , with different hierarchical basis in Figure 6. In Figure 6, one may find that as the order of hierarchical basis increases, the cutoff frequency of the numerical solutions increases. On the other hand, in the same process, the length of the region that has minimum phase/amplitude error is almost doubled, when each time a higher-order wavelet-like basis kicks in. These numerical results show that this hierarchical partition of unity can drastically improve the accuracy of the numerical solution of the Helmholtz equations.

## 3. NUMERICAL EXAMPLE II: HIGH-RESOLUTION SHEAR-BAND COMPUTATION

In this example, the meshless hierarchical basis is utilized to simulate shear-band formation numerically in an elasto-viscoplastic material. This problem has extensive engineering applications (see [9–13] and references therein). The idea to use spectral type of  $p$ -refinement to capture the localization mode is not new, which can be traced back to Belytschko *et al.* [14]. Because the localization zone is a region with high deformation gradient, a spectral overlay may properly represent the drastic change (high-frequency part) of the inelastic deformation. However, there are few differences between the spectral overlay technique and the wavelet-adaptive technique proposed here. In the spectral overlay technique, the spectral overlay is chosen to align in a given direction, which is supposed to be the eigen direction of the acoustic tensor when bifurcation occurs, and it is assumed to be given *a priori*; and the location of deployment of such spectral overlay is also prescribed. Moreover, the spectral function used in the overlay has little relations with the primary shape function basis, and thus carries no information on mesh organization/particle distribution, or the original interpolation process.

Contrast to the spectral overlay technique, the adaptive wavelet algorithm proposed here is more general in nature. The orientation of the wavelet basis is isotropic in space, and the enhancement of the numerical solution due to wavelet basis comes out naturally as the outcome of numerical computation, though the adaptive region are selected by a given criterion. Since the wavelet basis is intrinsically connected with the primary interpolation basis, the successive alternating  $h$ – $p$  refinement process may become efficient.

The model problem considered is the following tension test of an elasto-viscoplastic tensile bar, a rectangular specimen under plane strain tension (in reality, the plane stress tension test is probably more common). The prescribed displacement/velocity boundary condition is imposed at the both ends of the tensile bar as shown in Figure 7. The equilibrium equation, or the equation of motion is

$$\sigma_{ji,j} + b_i = \rho \dot{v}_i \quad (7)$$

where  $\sigma_{ij}$  is Cauchy stress,  $b_i$  is the body force,  $\rho$  is the density of the material, and  $v_i$  is the velocity of the continuum. For simplicity, the boundary conditions are specified with respect to the reference configuration,

$$\mathbf{P}\mathbf{n}_0 = \mathbf{T}^0, \quad \forall X \in \Gamma_X^T \quad (8)$$

$$\mathbf{u} = \mathbf{u}^0, \quad \forall X \in \Gamma_X^u \quad (9)$$

where  $\mathbf{P}$  is the first Piola–Kirchhoff stress tensor.

A rate form of constitutive relation is adopted,

$$\overset{\nabla}{\boldsymbol{\sigma}} := \mathbf{C}^{\text{elas}} (\mathbf{d} - \mathbf{d}^{\text{vp}}) \quad (10)$$

$$\dot{\boldsymbol{\sigma}} = \overset{\nabla}{\boldsymbol{\sigma}} + \mathbf{w}\boldsymbol{\sigma} + \boldsymbol{\sigma}\mathbf{w}^T \quad (11)$$

where  $\overset{\nabla}{\boldsymbol{\sigma}}$  is the Jaumann rate of Cauchy stress,  $\mathbf{C}^{\text{elas}}$  is the elastic modulus. The rate of deformation tensor,  $\mathbf{d}$ , and the spin tensor,  $\mathbf{w}$ , are defined as

$$\mathbf{d} := d_{ij}\mathbf{e}_i \otimes \mathbf{e}_j, \quad d_{ij} := \frac{1}{2} \left( \frac{\partial v_i}{\partial x_j} + \frac{\partial v_j}{\partial x_i} \right) \quad (12)$$



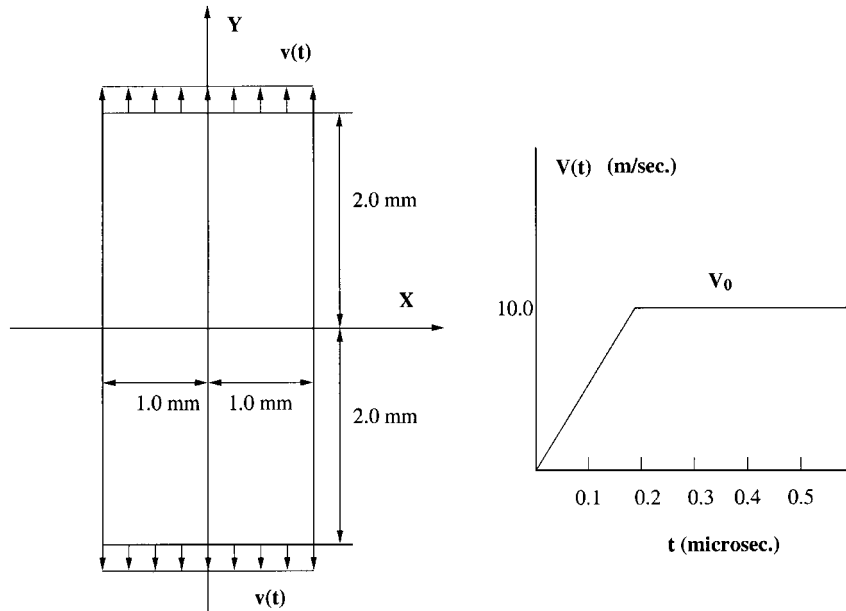


Figure 7. Description of model problem

$$\mathbf{w} := w_{ij} \mathbf{e}_i \otimes \mathbf{e}_j, \quad w_{ij} := \frac{1}{2} \left( \frac{\partial v_i}{\partial x_j} - \frac{\partial v_j}{\partial x_i} \right) \quad (13)$$

Followed Needleman [11], the von Mises yield condition is used to determine the flow direction and the rate of viscoplastic strain,

$$d_{ij}^{vp} := \bar{\eta}(\bar{\sigma}, \bar{\epsilon}) \frac{\partial f}{\partial \sigma_{ij}} \quad (14)$$

$$f(\boldsymbol{\sigma}, \kappa) = \bar{\sigma} - \kappa = 0 \quad (15)$$

The effective stress,  $\bar{\sigma}$ , and the effective viscoplastic strain,  $\bar{\epsilon}$ , are defined as

$$\bar{\sigma}^2 = \frac{3}{2} \mathbf{s} : \mathbf{s} \quad (16)$$

$$\bar{\epsilon} := \int_0^t \sqrt{\frac{2}{3} \mathbf{d}^{vp} : \mathbf{d}^{vp}} dt \quad (17)$$

where  $\mathbf{s}$  is the deviatoric stress tensor,

$$s_{ij} = \sigma_{ij} - \frac{1}{3} \text{tr}(\boldsymbol{\sigma}) \quad (18)$$

A power law is used to calculate the viscoplastic strain rate, i.e. in (14),

$$\bar{\eta} = \dot{\epsilon}_0 \left[ \frac{\bar{\sigma}}{g(\bar{\epsilon})} \right]^{1/m} \quad (19)$$

where

$$g(\bar{\varepsilon}) = \sigma_0 \frac{[1 + \bar{\varepsilon}/\varepsilon_0]^N}{1 + (\bar{\varepsilon}/\varepsilon_1)^2} \tag{20}$$

The variational (weak) form is stated as

$$\int_{\Omega_X} \rho_0 \ddot{u}_i \delta u_i \, d\Omega_X + \int_{\Omega_X} P_{Ji} \delta F_{Ji}^T \, d\Omega_X - \int_{\Omega_X} B_i \delta u_i \, d\Omega_X - \int_{\Gamma_X^T} T_i^0 \delta u_i \, d\Gamma = 0 \tag{21}$$

The following hierarchical reproducing kernel interpolants are used in the computation to simulate the shear-band formation

$$u_i^\rho(X) = \sum_{\ell=1}^{NP} \Psi_\ell^{[00]}(X) d_{i\ell}^{[00]}(t) + \sum_{|z|=1}^{\beta} \sum_{\ell=1}^{NAD} \Psi_\ell^{[z]}(X) d_{i\ell}^{[z]}(t) \tag{22}$$

where NP is the total number of particles, and NAD is the number of the particles at which the adaptive wavelet functions are added. The reproducing kernel hierarchical partition of unity used in this case is constructed as follows:

$$\Psi_\ell^{[z]}(x) := \mathbf{P} \left( \frac{x_\ell - x}{\varrho} \right) \mathbf{b}^{(\alpha)}(x) \phi_\varrho(x_\ell - x) \Delta V_\ell \tag{23}$$

In this case, the dimension of the space,  $n = 2$ , and  $\alpha = (0, 0), (1, 0), (0, 1), (1, 1)$ ; and  $x_\ell = (x_{1\ell}, x_{2\ell})$ ,  $x = (x_1, x_2)$ . The vector  $\mathbf{b}^{(\alpha)}(x)$  in (23) is determined by the moment equation

$$\begin{pmatrix} m_{00}^h & m_{10}^h & m_{01}^h & m_{11}^h \\ m_{10}^h & m_{20}^h & m_{11}^h & m_{21}^h \\ m_{01}^h & m_{11}^h & m_{02}^h & m_{12}^h \\ m_{11}^h & m_{21}^h & m_{12}^h & m_{22}^h \end{pmatrix} \begin{pmatrix} b_1^{(\alpha)} \\ b_2^{(\alpha)} \\ b_3^{(\alpha)} \\ b_4^{(\alpha)} \end{pmatrix} = \begin{pmatrix} \delta_{\alpha(0,0)} \\ \delta_{\alpha(1,0)} \\ \delta_{\alpha(0,1)} \\ \delta_{\alpha(1,1)} \end{pmatrix} \tag{24}$$

The 2-D cubic spline is used as the window functions. In all the calculations, we take  $a_x = a_y = 1.0$ . Substituting the reproducing kernel interpolants into the weak form, the discrete equations of motion can be put into the standard form

$$\mathbf{M} \ddot{\mathbf{d}} + \mathbf{f}^{\text{int}} = \mathbf{f}^{\text{ext}} \tag{25}$$

where  $\mathbf{M}$  is the mass matrix, and

$$\mathbf{f}_\ell^{\text{ext}} = \int_{\Gamma_X^T} T_i^0(X, t) \Phi_\ell(X) \mathbf{e}_i \, d\Gamma + \int_{\Omega_X} \rho_0 B_i(X, t) \Phi_\ell(X) \mathbf{e}_i \, d\Omega \tag{26}$$

$$\mathbf{f}_\ell^{\text{int}} = \int_{\Omega_X} P_{Ji} \frac{\partial \Phi_\ell}{\partial X_J} \mathbf{e}_i \, d\Omega \tag{27}$$

where

$$\{\Phi_\ell(X)\} = \{\{\Psi_\ell^{[00]}(X)\}, \{\Psi_\ell^{[10]}(X)\}, \{\Psi_\ell^{[01]}(X)\}, \{\Psi_\ell^{[11]}(X)\}\} \tag{28}$$

A forward gradient time integration scheme—the tangent modulus method proposed by Peirce *et al.* [15] is used as time integrator.

Since the wavelet basis constitute a partition of nullity, it introduces redundant degrees of freedom into the primary shape function basis. Consequently, the resulting stiffness matrix, and mass matrix are ill-conditioned. It should be noted that the spectral overlay method [14] introduces redundancy into the primary partition of unity as well, which is a possible source of pathology of numerical computation. To circumvent this difficulty, the inertia terms are neglected in the spectral overlay method, such that a set of semi-decoupled equilibrium equations can be obtained. A setback of this approach is that it only allows certain stress state within the spectral patch, regardless whether or not they have physical reality.

In this paper, only explicit integration scheme is adopted; therefore we face a problem to deal with a possible singular mass matrix. As a matter of fact, the mass matrix will become singular, if the conventional row summation, a lumped mass technique, is used; and the mass matrix will become extremely ill-conditioned when consistent mass matrix is employed. To circumvent this difficulty, the ‘special lumping technique’ proposed by Hinton *et al.* [16] is adopted.

The formula is

$$m_{ij}^s = \begin{cases} \omega \delta_{ij} \int_{\Omega_X} \rho_0 \Phi_j^2 \, d\Omega, & i = j \\ 0 & i \neq j \end{cases} \tag{29}$$

where

$$\omega := \frac{\int_{\Omega_X} \rho_0 \, d\Omega_X}{\left( \sum_{\ell=1}^{NP} \int_{\Omega_X} \rho_0 (\Psi_\ell^{[00]})^2 \, d\Omega + \sum_{|z|=1}^\beta \sum_{\ell}^{NAD} \int_{\Omega_X} \rho_0 (\Psi_\ell^{[z]})^2 \, d\Omega \right)} \tag{30}$$

The justification of Hinton’s special lumping technique is that it retains the diagonal part of the consistent mass matrix, and assumes that the diagonal part of the consistent mass matrix covers the correct frequency range of the dynamic response, whereas the non-diagonal part of the consistent mass matrix is not essential for the final results, at least not in quasi-static cases. This technique ensures the positive definiteness of the mass matrix, and eliminate the singular mode. A possible setback may be that it precludes the interaction between the neighbouring materials particles; however, this is compensated by the reproducing kernel formulation, because reproducing kernel particle method is a non-local interpolation process in principle.

The imperfections of the specimen are implanted for both geometric imperfection and the yield stress reduction. The distribution of yield stress reduction is given by the formula

$$\sigma_0(x_1, x_2) = \bar{\sigma}_Y [1.0 - \gamma \exp\{-[(x_1 - x_{c1})^2 + (x_2 - x_{c2})^2]/r_0^2\}] \tag{31}$$

where  $(x_{c1}, x_{c2})$  is the location of the imperfection, and  $\gamma, r_0$  are the magnitude and the size of the imperfection (Needleman [10]).

The geometric imperfection is implanted as the reduction in the width of the tensile bar. A linear distribution of reduction of width is imposed, the maximum reduction occurs at the middle section of the specimen (see Figure 9(c)).

Figures 8–13 contain a set of numerical results of four different tests. In the first example, there is no yield stress reduction at any point, only geometric imperfection is implanted. The width reduction at the middle section of specimen is 10 per cent, and the adaptive pattern is illustrated in Figure 9(c). The numerical results of the test are depicted in Figures 8 and 9. In

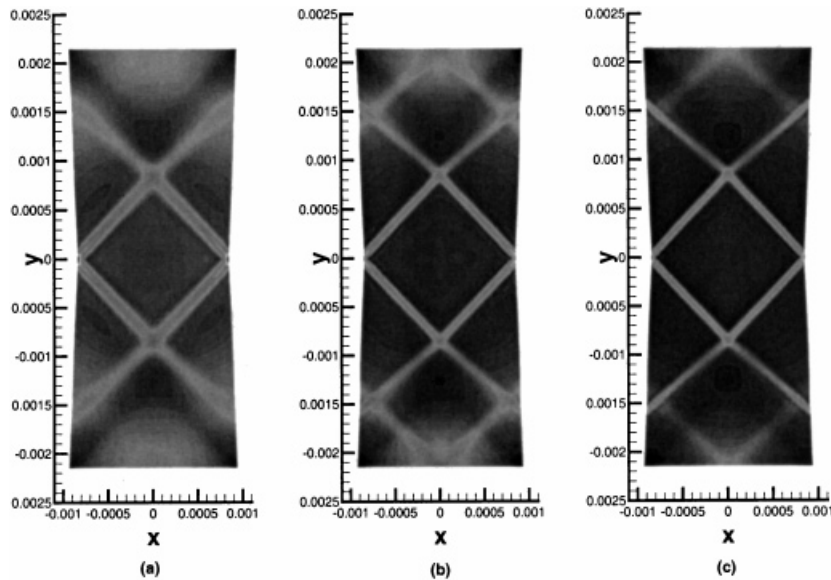


Figure 8. Test I: the contours of the viscoplastic strain in the tensile bar: (a) without wavelet adaptivity; (b) with wavelet adaptivity ( $\alpha = (1, 0), (0, 1)$ ); (c) with wavelet adaptivity ( $\alpha = (1, 0), (0, 1), (1, 1)$ )

the second test, both geometric imperfection as well as yield stress reduction are implanted. The geometric imperfection is the same as test I; and the yield stress reduction is prescribed according to equation (31), with  $\gamma = 0.1$  and  $x_{c1} = x_{c2} = 0$ . The results are depicted in Figure 10. In the third test, a smaller geometric imperfection is introduced, i.e. a 7.5 per cent reduction of width at the middle section of the specimen, while a yield stress reduction smeared through the centre with an intensity at  $\gamma = 0.2$ . The numerical results are displayed in Figure 11. In the fourth test, the geometric imperfection is even smaller, only a 1 per cent reduction of width at the middle of the specimen, and the yield stress reduction is the same as test III.

In all four numerical examples, 3321 particles are used in each computation. Since this is a bifurcation problem, which is characterized by the loss of ellipticity, the conventional indicators for elliptical differential equations break down. In this work, an intuitive adaptive criterion is adopted: we refine the regions, or the set of particles, that have the highest accumulated viscoplastic strain distribution. In the all four sets of numerical examples, the wavelet basis are added to 241 particles, which have the highest values of viscoplastic strain; subsequently, 482, or 723, new degrees of freedom are adding into the primary shape function basis. All the plots for the contours of accumulated viscoplastic strain are taken at time  $t = 16.8 \mu\text{s}$ ; and all the plots for the formation of shear band are taken at time,  $t = 24 \mu\text{s}$ . The key parameters used in computations are listed in Table I. In the computations, the following material parameters are used in all four tests  $\bar{\sigma}_Y = 460.0$  MPa,  $r_0 = 0.1$  mm,  $m = 0.01$ ,  $N = 0.1$ ,  $\varepsilon_0 = 2.18 \times 10^{-3}$ ,  $\varepsilon_1 = 100\varepsilon_0$  and  $\dot{\varepsilon}_0 = 0.002 \text{ s}^{-1}$ . One can observe that not only the width of the shear bands obtained from the wavelet adaptive solutions become thinner than the numerical solution without adaptivity, but also the finer features of those shear band come to earth. The numerical results in these four tests clearly demonstrate that the wavelet adaptive solutions provide the numerical solutions with much higher resolution than the numerical solution without wavelet adaptive refinement.

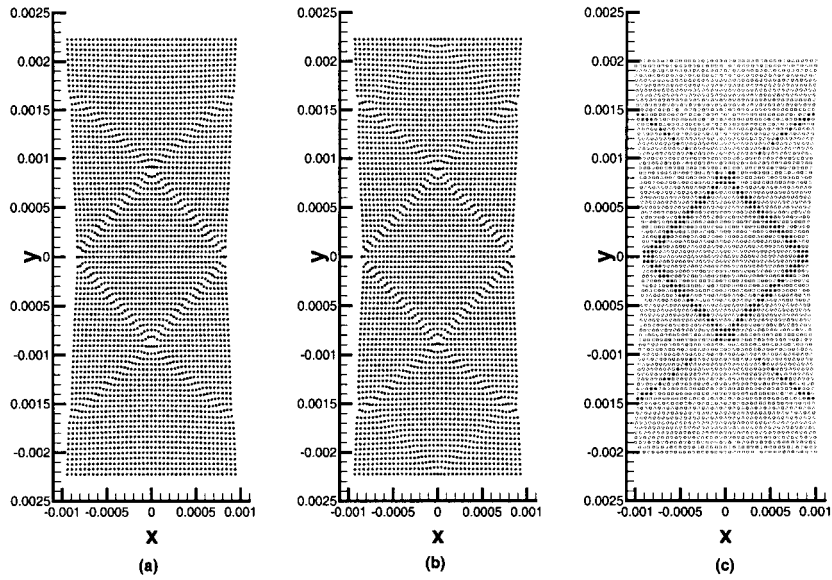


Figure 9. Test I: the shear band in the tensile bar represented by particle formation: (a) without wavelet adaptivity; (b) with wavelet adaptivity; (c) the adaptive pattern in undeformed configuration

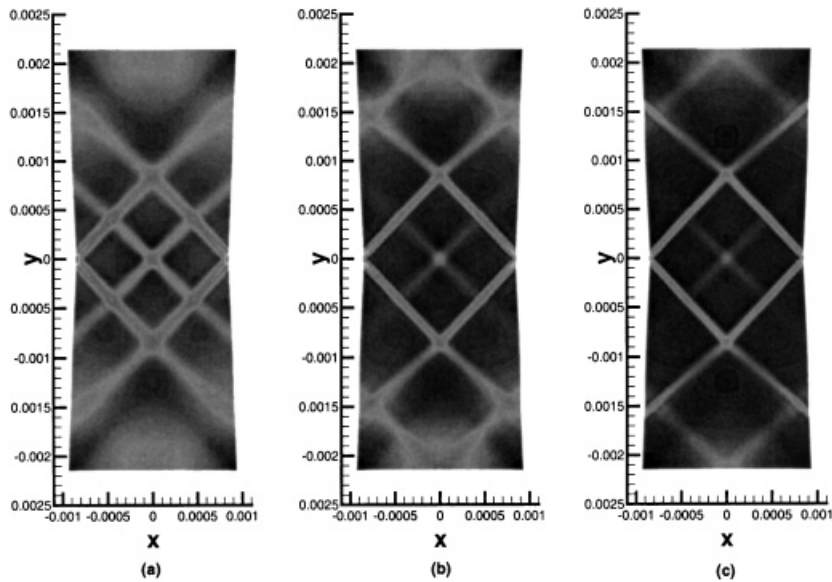


Figure 10. Test II: the contours of the viscoplastic strain in the tensile bar: (a) without wavelet adaptivity; (b) with wavelet adaptivity ( $\alpha = (1, 0), (0, 1)$ ); (c) with wavelet adaptivity ( $\alpha = (1, 0), (0, 1), (1, 1)$ )

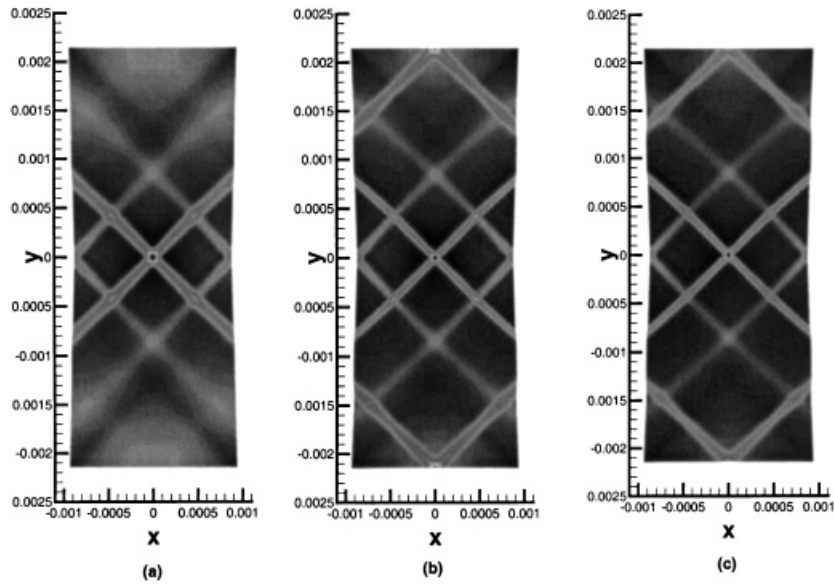


Figure 11. Test III: the contours of the viscoplastic strain in the tensile bar: (a) without wavelet adaptivity; (b) with wavelet adaptivity  $\alpha = (1, 0), (0, 1)$ ; (c) with wavelet adaptivity  $\alpha = (1, 0), (0, 1), (1, 1)$

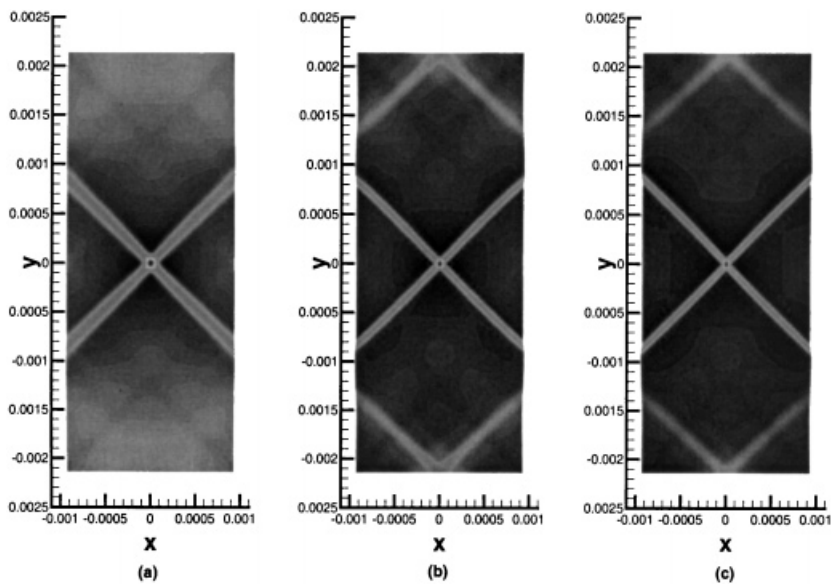


Figure 12. Test IV: the contours of the viscoplastic strain in the tensile bar: (a) without wavelet adaptivity; (b) with wavelet adaptivity  $\alpha = (1, 0), (0, 1)$ ; (c) with wavelet adaptivity  $\alpha = (1, 0), (0, 1), (1, 1)$

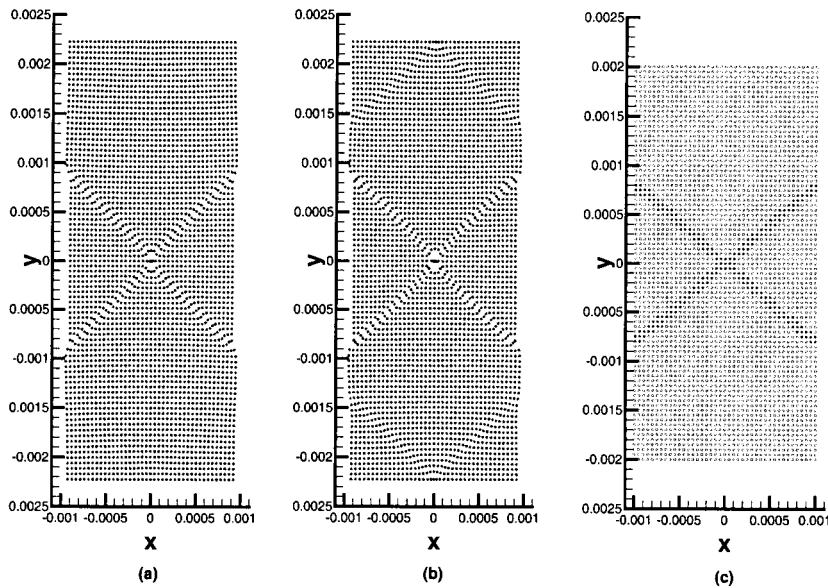


Figure 13. Test IV: the shear band in the tensile bar represented by particle formation: (a) without wavelet adaptivity; (b) with wavelet adaptivity; (c) the adaptive pattern in undeformed configuration

Table I. The parameters used in numerical tests (w: the reduction of the width at middle section of the specimen)

Test	$\gamma$	w	$dt (10^{-3} \mu s)$	$t (\mu s)$	NAD/NP
I	0.1	10%	1.5	24	241/3321
II	0.1	10%	1.5	24	241/3321
III	0.2	7.5%	1.5	24	241/3321
IV	0.2	1.0%	1.5	24	241/3321

The numerical simulation of shear-band formation via conventional finite element technique show a strong dependency of mesh orientation. As stated by Needleman [17], ‘*the ability of a finite element mesh to resolve localized shearing at angles oblique to the element boundary significantly affects the predicted course of shear-band development*’. As a meshless method, the reproducing kernel particle method has no explicit mesh, and therefore the issue of dependence on mesh orientation does not seem to exist. (There is another mesh sensitivity due to the loss of ellipticity of the governing equations, which does not occur in rate-dependent inelastic solid.) The previous best numerical results of tension test done by finite element methods are using the quadrilateral element consisting of four triangle elements with constant strain, whereas all the computations done here are just using uniform particle distribution with quadrilateral pattern. A detailed report on the relief of such mesh dependency by meshless method will be presented in a separate paper. The adaptive criterion used here is primitive, and it may be inadequate in some situations. There are some other adaptive criteria that can be used in the adaptive process of localization problem, such as the one proposed by Belytschko and Tabbara [18].

## 4. NUMERICAL EXAMPLE III: WAVELET PETROV–GALERKIN METHOD

In this section, the synchronized reproducing kernel interpolant constructed from the combination of wavelet kernels is used as a weighting function in a Petrov–Galerkin formulation to compute some typical pathological problems in numerical computations.

## 4.1. Advection–diffusion equations

We consider the following multiple dimensional advection–diffusion equation described as follows:

$$\mathcal{L}\varphi = -(\kappa_{ij}\varphi_{,j})_{,i} + u_i\varphi_{,i} = f, \quad \forall \mathbf{x} \in \Omega \quad (32)$$

$$\varphi = g, \quad \forall \mathbf{x} \in \Gamma_g \quad (33)$$

$$n_i\kappa_{ij}\varphi_{,j} = h, \quad \forall \mathbf{x} \in \Gamma_h \quad (34)$$

where  $\{\kappa_{ij}\}$  is the diffusivity, and  $\{u_i\}$  is the given velocity of the flow field.

Define

$$(f, g) := \int_{\Omega} fg \, d\Omega \quad (35)$$

$$\mathbf{B}(w, \varphi) := \int_{\Omega} (wu_{,i}\varphi_{,i} + w_{,i}\kappa_{ij}\varphi_{,j}) \, d\Omega \quad (36)$$

$$\mathbf{L}(w) := \int_{\Omega} wf \, d\Omega + \int_{\Gamma_h} wh \, d\Gamma_h \quad (37)$$

Let

$$\varphi^h(\mathbf{x}) := \sum_{I \in \Lambda} \varphi_I^h \Psi_I^{[00]}(\mathbf{x}) \quad (38)$$

$$w^h(\mathbf{x}) := \sum_{I \in \Lambda} c_I \Psi_I^{[00]}(\mathbf{x}) \quad (39)$$

$$\bar{w}^h(\mathbf{x}) := w^h(\mathbf{x}) + \tau \tilde{w}^h(\mathbf{x}) \quad (40)$$

where  $\tau$  is a stability control parameter and is  $\mathcal{O}(1)$ .

For  $|\beta| = 1$  ( $\beta = (1, 0), (0, 1)$ )

$$\tilde{w}^h(\mathbf{x}) := \hat{u}_j \tilde{w}_j^h(\mathbf{x}) \quad (41)$$

$$\tilde{w}_j^h(\mathbf{x}) := \sum_{I \in \Lambda} c_I \Psi_I^{[\beta_j]}(\mathbf{x}) \quad (42)$$

$$\hat{u}_j := \frac{u_j}{\|u\|} \quad \text{and} \quad \|u\|^2 := u_i u_i \quad (43)$$

where  $0 \leq j \leq n$  and  $|\beta_j| = 1$ .

Then, a consistent weighted residual form is

$$(\bar{w}^h, \mathcal{L}\varphi^h - f) = 0 \quad (44)$$

Integration by parts yields the weak formulation

$$\mathbf{B}(\bar{w}^h, \varphi^h) - \int_{\Gamma_g} \bar{w}^h n_i \kappa_{ij} \varphi_{,j}^h \, d\Gamma_g = \mathbf{L}(\bar{w}^h) \quad (45)$$



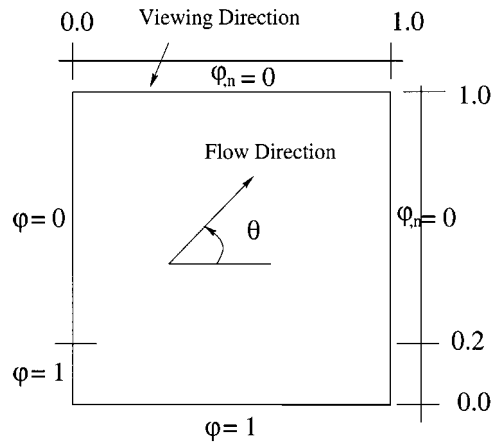


Figure 14. Advection skew to the ‘mesh’: problem statement

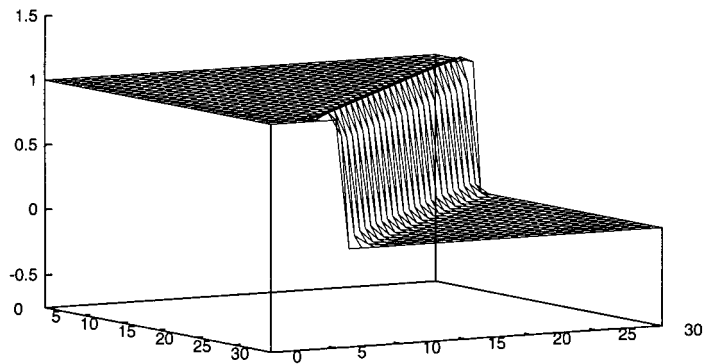


Figure 15. Numerical results for advection skew to the ‘mesh’ via wavelet Petrov–Galerkin

where  $\bar{w}^h$  is a synchronized interpolant. The first numerical test is the so-called advection skew to the ‘mesh’. The problem statement is described in Figure 14, and the result is displayed in Figure 15. In Figure 15, an uniform particle distribution,  $21 \times 21$ , is used; no shock capturing term is involved. The results show that the numerical solutions are stable.

The second test is the so-called cosine hill problem—advection in a rotating flow field. The numerical results are shown in Figure 16. Part (a) of Figure 16 displays the profile of the function  $\varphi$ , and the part (b) of the figure shows the contour of advection–diffusion field  $\varphi$ . The computation is performed on a  $30 \times 30$  particle distribution. In Figure 16, one can observe that there is no phase error in numerical results. In both cases, the diffusive coefficient  $\kappa$  is taken as  $10^{-6}$ . A proof of stability and convergence for using the above wavelet Petrov–Galerkin method in numerical computation of advection–diffusion problem is presented in the next section.

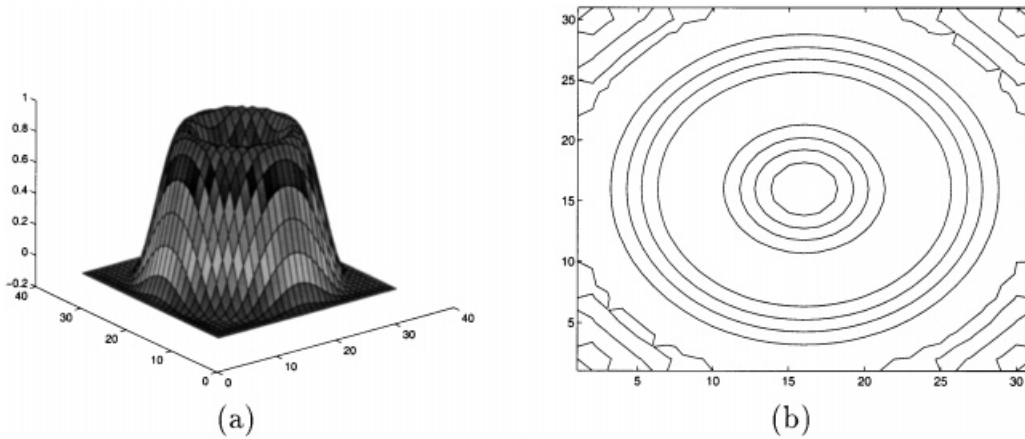


Figure 16. Numerical results for advection in a rotating field: (a) the profile of  $\varphi$ ; (b) the contours of  $\varphi$

#### 4.2. Stokes flow problem

The mathematical formulation of the problem is as follows:

$$\nabla \cdot \boldsymbol{\sigma} + \mathbf{f} = \mathbf{0} \tag{46}$$

$$\nabla \cdot \mathbf{u} = 0 \tag{47}$$

where

$$\boldsymbol{\sigma} = -p\mathbf{I} + 2\mu\boldsymbol{\varepsilon}, \quad \boldsymbol{\varepsilon} = \frac{1}{2}(\nabla\mathbf{u} + (\nabla\mathbf{u})^t)$$

with the boundary conditions

$$\mathbf{u}(\mathbf{x}) = \mathbf{g}(\mathbf{x}) \quad \forall \mathbf{x} \in \Gamma_g \tag{48}$$

$$(\boldsymbol{\sigma} \cdot \mathbf{n})(\mathbf{x}) = \mathbf{h}(\mathbf{x}) \quad \forall \mathbf{x} \in \Gamma_h \tag{49}$$

It is well known that the velocity-based computational formulation of the Stokes flow problem suffers from instability in numerical simulations, if the conventional Bubnov–Galerkin procedure is adopted. An efficient remedy in computational strategy is to use the so-called mixed method. However, in a mixed formulation, there are certain restrictions that have to be met for displacement interpolation and pressure interpolation. The celebrated Babuška–Brezzi condition is such a requirement imposed by stability criterion. For example, it excludes the convenient equal-order interpolation in computations. Hughes *et al* [32], proposed a Petrov–Galerkin formulation to circumvent the Babuška–Brezzi Condition (CBB), such that any consistent interpolation schemes can be employed in computations. Here, following almost the exact same Petrov–Galerkin formulation, we use the synchronized reproducing kernel interpolant as weighting function in the computation, instead of using the gradient of the pressure trial function as proposed in Hughes’ formulation. Assume that the set  $\Lambda$  can be decomposed as<sup>‡</sup>

$$\Lambda = \overset{\circ}{\Lambda} \oplus \partial\Lambda \tag{50}$$

<sup>‡</sup>This is not always possible in multiple dimensional problems; see discussion in [19]

where

$$\overset{\circ}{\Lambda} := \{I \in \Lambda, \Psi_I^{[00]}(\mathbf{x}) = 0, \forall \mathbf{x} \in \partial\Omega\} \tag{51}$$

$$\partial\Lambda := \{I \in \Lambda, \Psi_I^{[00]}(\mathbf{x}) \neq 0, \forall \mathbf{x}_I \in \partial\Omega\} \tag{52}$$

We choose the following equal-order interpolation for both displacements and pressure:

$$\mathbf{u}^h(\mathbf{x}) := \sum_{I \in \overset{\circ}{\Lambda}} \mathbf{u}_I \Psi_I^{[00]}(\mathbf{x}) + \sum_{I \in \partial\Lambda} \mathbf{g}_I \Psi_I^{[00]}(\mathbf{x}) = \mathbf{v}^h(\mathbf{x}) + \mathbf{g}^h(\mathbf{x}) \tag{53}$$

$$\mathbf{w}^h(\mathbf{x}) := \sum_{I \in \overset{\circ}{\Lambda}} \mathbf{w}_I \Psi_I^{[00]}(\mathbf{x}) \tag{54}$$

and

$$p^h(\mathbf{x}) := \sum_{I \in \Lambda} p_I \Psi_I^{[00]}(\mathbf{x}) \tag{55}$$

$$q^h(\mathbf{x}) := \sum_{I \in \Lambda} q_I \Psi_I^{[00]}(\mathbf{x}) \tag{56}$$

For  $\beta = 1$ , let

$$\tilde{\mathbf{q}}^h(\mathbf{x}) := \{\tilde{q}_1^h(\mathbf{x}), \tilde{q}_2^h(\mathbf{x})\} \tag{57}$$

$$\tilde{q}_j^h(\mathbf{x}) := \frac{q_j}{2\mu} \sum_{I \in \Lambda} \tilde{q}_{Ij} \Psi_I^{[\beta_j]}(\mathbf{x}), \quad j = 1, 2 \tag{58}$$

where there is no summation on  $j$ , and in 2-D

$$\beta_j = (1, 0), (0, 1) \tag{59}$$

Then, the following CBB type of Petrov–Galerkin weak form is used in the computation:

$$\mathbf{B}_\tau(\mathbf{w}^h, \mathbf{q}^h, \tilde{\mathbf{q}}^h; \mathbf{v}^h, \mathbf{p}^h) = \mathbf{L}_\tau(\mathbf{w}^h, \mathbf{q}^h, \tilde{\mathbf{q}}^h) \tag{60}$$

where

$$\begin{aligned} \mathbf{B}_\tau(\mathbf{w}^h, \mathbf{q}^h, \tilde{\mathbf{q}}^h; \mathbf{v}^h, \mathbf{p}^h) &:= (\varepsilon(\mathbf{w}^h), 2\mu\varepsilon(\mathbf{v}^h)) - (\nabla \cdot \mathbf{w}^h, \mathbf{p}^h) + (\mathbf{q}^h, \nabla \cdot \mathbf{v}^h) \\ &\quad + (\tau\tilde{\mathbf{q}}^h, \nabla p^h - 2\mu\nabla \cdot \varepsilon(\mathbf{v}^h)) \end{aligned} \tag{61}$$

$$\begin{aligned} \mathbf{L}_\tau(\mathbf{w}^h, \mathbf{q}^h, \tilde{\mathbf{q}}^h) &:= (\mathbf{w}^h + \tau\tilde{\mathbf{q}}^h, \mathbf{f}) + (\mathbf{w}^h, \mathbf{h})_{\Gamma_n} - (\varepsilon(\mathbf{w}^h), 2\mu\varepsilon(\mathbf{g}^h)) \\ &\quad - (q^h, \nabla \cdot \mathbf{g}^h) + (\tau\tilde{\mathbf{q}}^h, 2\mu\nabla \cdot \varepsilon(\mathbf{g}^h)) \end{aligned} \tag{62}$$

where  $\tau$  is the stability control parameter.

In numerical experiments, the well-known cavity problem is tested. It is a driven cavity flow problem with ‘leaky lid’ boundary condition. The problem statement is shown in Figure 17. The synchronized reproducing kernel interpolants developed in Section 3 are employed in the computation. The results presented in Figures 18 and 19 are based on a  $11 \times 11$  particle distribution on an unit square. In all the computations, 2-D cubic spline is used as the window function, and the dilation vector is chosen as  $q_1 = 1 \cdot h_{x_1}$ ,  $q_2 = 1 \cdot h_{x_2}$ . Figure 18 shows the pressure profile of the cavity problem. Part (a) is the numerical result obtained from Petrov–Galerkin formulation based on Equation (60). Part (b) is the numerical result obtained from regular Galerkin method, from which, the pressure distribution exhibits apparent spurious pressure mode. In Figure 19, the pressure contour and the velocity field, or the field of streamline, are displayed; both of them are obtained from the Petrov–Galerkin formulation (60).

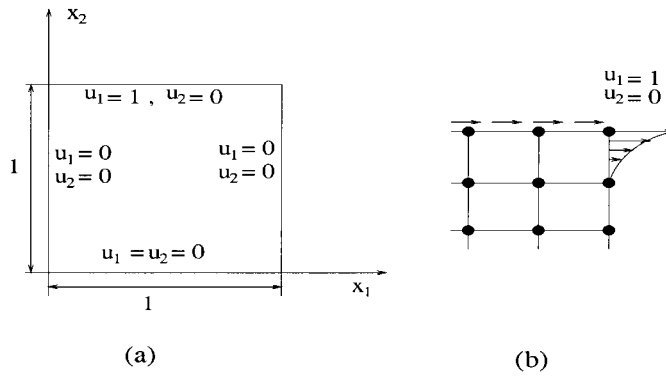


Figure 17. The cavity problem: (a) problem statement; (b) detailed boundary conditions at the corner

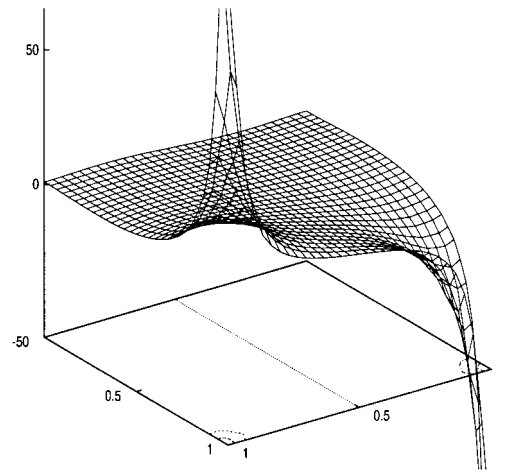


Figure 18. Pressure elevation: Petrov-Galerkin solution

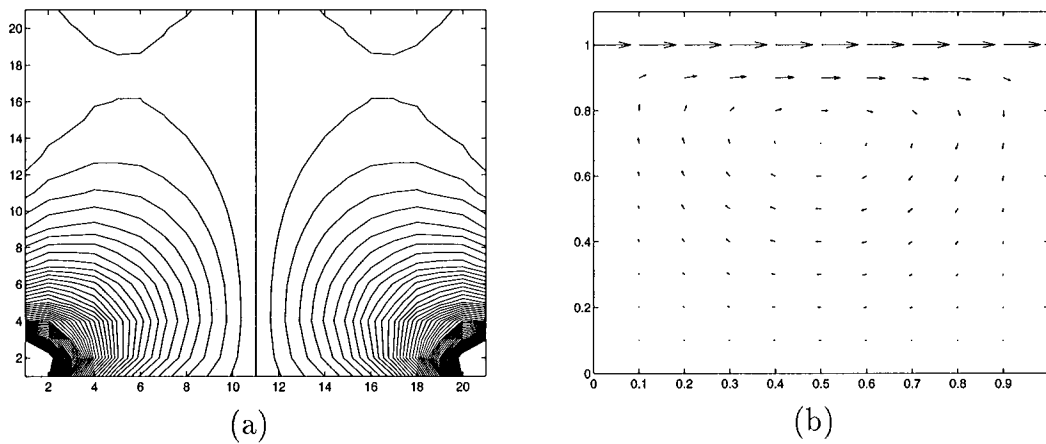


Figure 19. Numerical results of cavity problem: (a) pressure contours; (b) velocity field

5. STABILITY AND CONVERGENCE OF WAVELET PETROV–GALERKIN METHOD

In this section, the stability and convergence of the proposed wavelet Petrov–Galerkin method is sketched for a 1-D advection–diffusion problem, which are, in most part, similar to the standard results by Johnson *et al.* [19, 20] and Hughes *et al.* [21–24]. As a matter of fact, the main philosophy of the proof and much of the technicalities involved here directly comes from an excellent monograph by Hughes *et al.* [25]. Nevertheless, there are some unusual spots, such as: (1) the weighting function is considered as an synchronized reproducing kernel interpolant that is introduced in Section 4 and (2) the algorithm is a global, continuous approach; no discontinuous Galerkin argument is necessary.

5.1. Model problem

We consider the following 1-D advective–diffusive problem as the model problem:

$$-\kappa\varphi_{,xx} + a\varphi_{,x} = f, \quad x \in (0, L) \subset \mathbb{R} \tag{63}$$

$$\varphi(0) = \varphi_0, \quad \varphi(L) = \varphi_L \tag{64}$$

where  $\varphi_{,x} := d\varphi/dx$ ,  $\varphi_{,xx} := d^2\varphi/dx^2$ , and the source term  $f(x)$  is given for  $x \in [0, L]$ . In (63),  $\kappa$  is the diffusive coefficient, and  $a$  is the advection velocity; both of them are positive constants.

Let  $\mathcal{D} := \{x_I \mid 0 \leq x_I \leq L, I = 1, \dots, np\}$  and define function spaces:

$$\mathcal{V}^\varrho := \{w^\varrho \mid w^\varrho \in H_0^1([0, L]) \text{ and } w^\varrho \in \text{span} \{\Psi_I^{[0]}(x)\}\} \tag{65}$$

$$\mathcal{F}^\varrho := \{\varphi^\varrho \mid \varphi^\varrho \in H^1([0, L]) \text{ and } \varphi^\varrho \in \text{span} \{\Psi_I^{[0]}(x)\}\} \tag{66}$$

$$\mathcal{V}_1^\varrho := \{\tilde{w}^\varrho \mid \tilde{w}^\varrho \in H^1([0, L]) \text{ and } \tilde{w}^\varrho \in \text{span} \{\Psi_I^{[1]}(x)\}\} \tag{67}$$

We assume that there exists index set  $A \subset \subset \Lambda$  such that

$$w^\varrho(x) = \sum_{I \in A} w_I^\varrho \Psi_I^{[0]}(x) \tag{68}$$

where

$$A := \{I \in \Lambda \mid \Psi_I^{[0]}(0) = \Psi_I^{[0]}(L) = 0\}^\S$$

and

$$\varphi^\varrho(x) := \sum_{I \in \Lambda} \varphi_I^c \Psi_I^{[0]}(x) = \sum_{I \in A} \varphi_I^c \Psi_I^{[0]}(x) + \varphi_0 g_0(x) + \varphi_L g_L(x) \tag{69}$$

$$\tilde{w}^\varrho(x) = \sum_{I \in A} w_I^c \Psi_I^{[1]}(x) \tag{70}$$

where  $g_0(0) = 1, g_0(L) = 0$ ; and  $g_L(0) = 0, g_L(L) = 1$ .

Let  $w_p(x) := w^\varrho(x) + \tau \text{sgn}(a)\tilde{w}^\varrho(x)$ , where  $\tau$  is a stability control parameter. We consider the following algorithm:

*Algorithm 5.1.* Find  $\varphi^\varrho \in \mathcal{F}^\varrho, \forall w^\varrho \in \mathcal{V}^\varrho$  and the associated  $\tilde{w}^\varrho \in \mathcal{V}_1^\varrho$ , such that

$$\int_0^L (-a\varphi^\varrho w_{,x}^\varrho + \kappa w_{,xx}^\varrho \varphi^\varrho) \, dx + \text{sgn}(a) \tau \int_0^L \tilde{w}^\varrho (-\kappa\varphi_{,xx}^\varrho + a\varphi_{,x}^\varrho - f) \, dx = \int_0^L w^\varrho f \, dx \tag{71}$$

<sup>§</sup>This is always possible in one-dimensional particle distribution; (See [26])

Define the bilinear form

$$B(u, v) := \int_0^L (-\kappa u_{,xx} + au_{,x})v \, dx \tag{72}$$

$\forall w^\rho \in \mathcal{V}^\rho$ ,

$$B(w^\rho, w^\rho) = \int_0^L (-\kappa w_{,xx}^\rho + aw_{,x}^\rho)w^\rho \, dx = \int_0^L (\kappa(w_{,x}^\rho)^2 + a \frac{d}{dx}(w^\rho)^2) \, dx = \kappa \|w_{,x}^\rho\|_{L^2([0,L])}^2 \tag{73}$$

and

$$\begin{aligned} B_{\text{WPG}}(w^\rho; \tilde{w}^\rho) &:= B(w^\rho, w^\rho) + \text{sgn}(a)\tau \int_0^L (-\kappa w_{,xx}^\rho + aw_{,x}^\rho)\tilde{w}^\rho \, dx \\ &= \kappa \|w_{,x}^\rho\|_{L^2(\Omega)}^2 + \tau|a|(w_{,x}^\rho, \tilde{w}^\rho) - \kappa\tau \text{sgn}(a)(w_{,xx}^\rho, \tilde{w}^\rho) \end{aligned} \tag{74}$$

### 5.2. Stability and convergence of wavelet Petrov–Galerkin method

To set the stage, we proceed by listing several inequalities, including the inverse estimate for the reproducing kernel approximation and the wavelet estimate.

*Inequality 5.1.* Let  $\varepsilon > 0$  and  $f(x), g(x) \in L^2(\Omega)$ . One has

$$|(f, g)| \leq \frac{1}{2} \left( \frac{1}{\varepsilon} \|f\|_{L^2(\Omega)}^2 + \varepsilon \|g\|_{L^2(\Omega)}^2 \right) \tag{75}$$

*Inequality 5.2 (Inverse estimate).*  $\forall v^\rho \in \text{span} \{ \Psi_I^{[0]}(x) \}$ , namely,

$$v^\rho(x) := \sum_{I \in \Lambda} v_I \mathcal{K}_\rho^{[0]}(x_I - x, x) \Delta x_I \tag{76}$$

there exists  $C > 0$ , such that  $|\gamma| \geq |\alpha|$  the following inequality holds

$$\|v^\rho\|_{H^{|\gamma|}(\Omega)} \leq C_I \rho^{|\alpha| - |\gamma|} \|v^\rho\|_{H^{|\alpha|}(\Omega)}, \quad |\alpha|, |\gamma| \leq m \tag{77}$$

*Proof.* The proof follows from Brenner and Scott [27] almost verbatim, except that this is a direct global estimate. Let

$$\zeta := \frac{x}{\rho} \Rightarrow \hat{v}(\zeta) := v(\rho\zeta); \quad \Delta V_{\zeta I} = \frac{1}{\rho^n} \Delta V_I$$

and define

$$\hat{v}^\rho(\zeta) := \mathcal{R}_{1,h}^{m,[0]} \hat{v} = \sum_{I \in \Lambda} \mathcal{K}^{[0]}(\zeta_I - \zeta, \zeta) \hat{v}_I \Delta V_{\zeta I} \tag{78}$$

By homogeneous argument,

$$|\hat{v}^\rho|_{H^{|\beta|}(\hat{\Omega})} = \rho^{|\beta| - n/2} |v^\rho|_{H^{|\beta|}(\Omega)}, \quad |\alpha| \leq m \tag{79}$$

Furthermore, since  $\mathcal{V}^\rho$  is finite dimensional; by equivalence of the norms

$$\|\hat{v}^\rho\|_{H^{|\beta|}(\hat{\Omega})} \leq C \|v^\rho\|_{L^2(\hat{\Omega})} \tag{80}$$

Equation (80) implies that  $\exists C > 0$  such that

$$|v^\rho|_{H^j(\Omega)} \leq C \rho^{-j} \|v^\rho\|_{L^2(\Omega)}, \quad 0 \leq j \leq |\beta| \tag{81}$$

Since  $\rho \leq 1$ , we have

$$\|v^\rho\|_{H^{|\beta|}(\Omega)} \leq C \rho^{-|\beta|} \|v^\rho\|_{L^2(\Omega)}, \quad |\beta| \leq m \tag{82}$$

Now, assume  $\gamma = \alpha + \beta$ . Then

$$\begin{aligned} \|D^\gamma v^\rho\|_{L^2(\Omega)} &\leq C \|D^\alpha v^\rho\|_{H^{|\beta|}(\Omega)} \\ &\leq C \rho^{-|\beta|} \|D^\alpha v^\rho\|_{L^2(\Omega)} \\ &\leq C \rho^{-|\beta|} |v^\rho|_{H^{|\alpha|}(\Omega)} \end{aligned} \tag{83}$$

Since  $|\beta| = |\gamma| - |\alpha|$ , it is straightforward that

$$|v^\rho|_{H^{|\gamma|}(\Omega)} \leq C \rho^{|\alpha| - |\gamma|} |v^\rho|_{H^{|\alpha|}(\Omega)} \tag{84}$$

Equation (77) follows consequently. □

*Inequality 5.3 (Wavelet estimate). Define*

$$w^\rho(x) = \sum_{I \in \Lambda} w_I^c \Psi_I^{[0]}(x) \tag{85}$$

$$\tilde{w}^\rho(x) = \sum_{I \in \Lambda} w_I^c \Psi_I^{[1]}(x) \tag{86}$$

$\forall w^c \in \text{span}\{\Psi_I^{[0]}(x)\}$ , assume

$$\|w_{,xx}^c\|_{L^2([0,L])} \leq C_D \|w_{,xx}^\rho\|_{L^2([0,L])} \tag{87}$$

Then  $\exists C_B > 0$  such that the following estimate holds:

$$\|w_{,x}^\rho - \tilde{w}^\rho/\varrho\|_{L^2([0,L])} \leq C_B \varrho \|w_{,xx}^\rho\|_{L^2([0,L])} \tag{88}$$

*Proof.* For  $m \geq 1$ , Theorem (4.1) in Part I asserts that  $\exists C_1, C_2 > 0$  such that

$$\|w_{,x}^c - w_{,x}^\rho\|_{L^2([0,L])} \leq C_1 \rho |w^c|_{H^2([0,L])} \tag{89}$$

$$\|w_{,x}^c - \tilde{w}^\rho/\varrho\|_{L^2([0,L])} \leq C_2 \rho |w^c|_{H^2([0,L])} \tag{90}$$

therefore

$$\begin{aligned} \|w_{,x}^\rho - \tilde{w}^\rho/\varrho\|_{L^2([0,L])} &= \|(w_{,x}^\rho - w_{,x}^c) + (w_{,x}^c - \tilde{w}^\rho/\varrho)\|_{L^2([0,L])} \\ &\leq \|w_{,x}^\rho - w_{,x}^c\|_{L^2([0,L])} + \|w_{,x}^c - \tilde{w}^\rho/\varrho\|_{L^2([0,L])} \\ &\leq (C_1 + C_2) \varrho \|w_{,xx}^c\|_{L^2([0,L])} \\ &\leq (C_1 + C_2) C_D \varrho \|w_{,xx}^\rho\|_{L^2([0,L])} \end{aligned} \tag{91}$$

Choosing  $C_B = (C_1 + C_2) C_D$  yields (88). □

*Remark 5.1* (1) The reason that this estimate holds is because  $D_{x/\rho}\mathcal{H}_\varrho^{[0]}(x_I - x, x)$  and  $\mathcal{H}_\varrho^{[1]}(x_I - x, x)$  share the same differential consistency condition; (2) if  $w^\varepsilon(x) \in C^2([0, L])$ ,  $C_D = 1$ ; (3) it is apparent that when  $m > 1$ ,  $C_B \ll 1$ . In the rest of the proof, we assume that  $C_B \ll 1$ .

By stability we mean the coerciveness of the bilinear form  $B_{\text{WPG}}(w^\varepsilon; \tilde{w}^\varepsilon)$ .

*Theorem 5.1 (Stability).*  $\forall w^\varepsilon \in \mathcal{V}^\varepsilon$ , the bilinear form based on wavelet Petrov–Galerkin algorithm (5.1) is uniformly coercive, namely

$$B_{\text{WPG}}(w^\varepsilon; \tilde{w}^\varepsilon) \geq C_c \tag{92}$$

where  $C_c > 0$  is independent of  $\kappa$ .

*Proof.* By definition,

$$\begin{aligned} B_{\text{WPG}}(w^\varepsilon; \tilde{w}^\varepsilon) &= \kappa \|w_{,x}^\varepsilon\|_{L^2([0,L])}^2 + \tau |a|(w_{,x}^\varepsilon, \tilde{w}^\varepsilon) - \tau \kappa \operatorname{sgn}(a)(w_{,xx}^\varepsilon, \tilde{w}^\varepsilon) \\ &= \kappa \|w_{,x}^\varepsilon\|_{L^2([0,L])}^2 + \tau |a| \varrho (w_{,x}^\varepsilon, w_{,x}^\varepsilon) \\ &\quad - \tau \kappa \varrho \operatorname{sgn}(a)(w_{,xx}^\varepsilon, w_{,x}^\varepsilon) - \tau |a| \varrho (w_{,x}^\varepsilon, w_{,x}^\varepsilon - \tilde{w}^\varepsilon/\varrho) \\ &\quad + \tau \kappa \varrho \operatorname{sgn}(a)(w_{,xx}^\varepsilon, w_{,x}^\varepsilon - \tilde{w}^\varepsilon/\varrho) \end{aligned} \tag{93}$$

Utilizing inequality (75), it is straightforward that

$$\begin{aligned} B_{\text{WPG}}(w^\varepsilon; \tilde{w}^\varepsilon) &\geq \kappa \|w_{,x}^\varepsilon\|_{L^2([0,L])}^2 + \tau |a| \varrho \|w_{,x}^\varepsilon\|_{L^2([0,L])}^2 - \frac{\tau \kappa \varrho}{2} \left( \frac{1}{\varepsilon} \|w_{,x}^\varepsilon\|_{L^2([0,L])}^2 + \varepsilon \|w_{,xx}^\varepsilon\|_{L^2([0,L])}^2 \right) \\ &\quad - \tau |a| \varrho \|w_{,x}^\varepsilon\|_{L^2([0,L])} \|w_{,x}^\varepsilon - \tilde{w}^\varepsilon/\varrho\|_{L^2([0,L])} - \tau \kappa \varrho \|w_{,xx}^\varepsilon\|_{L^2([0,L])} \|w_{,x}^\varepsilon - \tilde{w}^\varepsilon/\varrho\|_{L^2([0,L])} \end{aligned} \tag{94}$$

Apply the inverse estimate (77) and the wavelet estimate (88)–(94),

$$\begin{aligned} B_{\text{WPG}}(w^\varepsilon; \tilde{w}^\varepsilon) &\geq \kappa \|w_{,x}^\varepsilon\|_{L^2([0,L])}^2 + \tau |a| \varrho \|w_{,x}^\varepsilon\|_{L^2([0,L])}^2 - \frac{\tau \kappa \varrho}{2} \left( \frac{1}{\varepsilon} + \varepsilon \varrho^{-2} C_I^2 \right) \|w_{,x}^\varepsilon\|_{L^2([0,L])}^2 \\ &\quad - C_B \tau |a| \varrho^2 \|w_{,x}^\varepsilon\|_{L^2([0,L])} \|w_{,xx}^\varepsilon\|_{L^2([0,L])} - C_B \tau \kappa \varrho^2 \|w_{,xx}^\varepsilon\|_{L^2([0,L])}^2 \\ &\geq \left( \kappa - \frac{\tau \kappa \varrho}{2\varepsilon} - C_B C_I^2 \kappa \tau - \frac{\tau \kappa \varepsilon}{2\varrho} C_I^2 \right) \|w_{,x}^\varepsilon\|_{L^2([0,L])}^2 \\ &\quad + \tau |a| \varrho (1 - C_B C_I) \|w_{,x}^\varepsilon\|_{L^2([0,L])}^2 \end{aligned} \tag{95}$$

Choosing  $\varepsilon = \tau \varrho$ , one has

$$B_{\text{WPG}}(w^\varepsilon; \tilde{w}^\varepsilon) \geq \left\{ \frac{\kappa}{2} (1 - 2C_B C_I^2 \tau - C_I^2 \tau^2) + \tau |a| \varrho (1 - C_B C_I) \right\} \|w_{,x}^\varepsilon\|_{L^2([0,L])}^2 \tag{96}$$

Define

$$Y(\tau) = 1 - 2C_B C_I^2 \tau - C_I^2 \tau^2 \tag{97}$$

There are two distinct roots for equation  $Y(\tau) = 0$ ,

$$\tau_\pm := C_B \pm \sqrt{C_B^2 + C_I^{-2}} \tag{98}$$

In Figure (20), the function  $Y(\tau)$  is plotted against  $\tau$  for  $C_B = 0.01$  and  $C_I = 2.0$ .



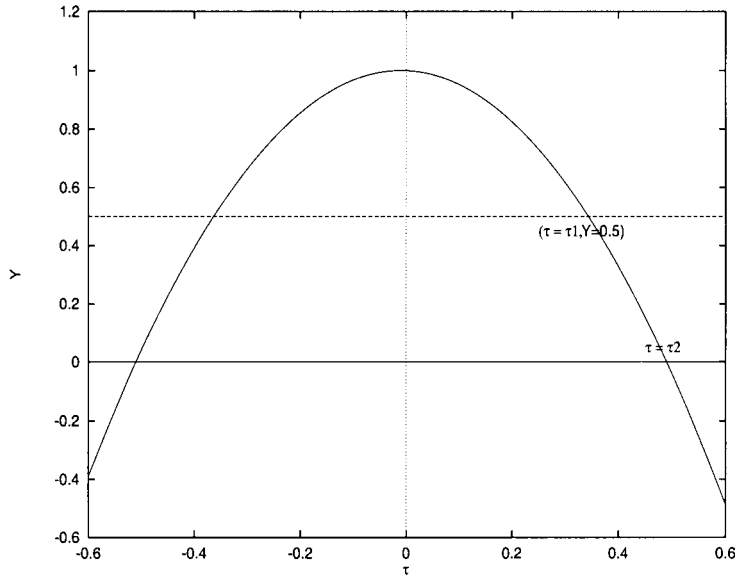


Figure 20.  $Y(\tau)$  at  $a = 1.0$ ,  $C_B = 0.01$ ,  $C_I = 2.0$

By the assumption that  $C_B C_I \ll 1$ , to meet the condition that

$$B_{\text{WPG}}(w^\ell; \tilde{w}^\ell) > 0 \tag{99}$$

we have to enforce  $Y(\tau) \geq 0$  and  $\tau(1 - C_B C_I) > 0$ . This requires that  $0 < \tau < \tau_2$ , where

$$\tau_2 := C_B + \sqrt{C_B^2 + C_I^{-2}} \tag{100}$$

Choosing  $\tau = \tau_2$ , we then have

$$B_{\text{WPG}}(w^\ell; \tilde{w}^\ell) \geq \varrho |a| \tau_2 \|w_{,x}^\ell\|_{L^2([0,L])}^2 = C_c > 0 \tag{101}$$

It should be noted that  $\varrho \|w_{,x}^\ell\|_{L^2([0,L])}^2 \sim O(\varrho^{-1})$ . Thus, the estimate is uniform in  $\kappa$ . □

*Theorem 5.2 (Convergence).* For the model problem (63) and (64), by using the wavelet packet generated by a  $m$ th order polynomial basis in the variational form (5.1), namely  $\mathcal{X}_\varrho^{[0]}(\cdot, \cdot)$  and  $\mathcal{X}_\varrho^{[1]}(\cdot, \cdot)$ . The error for the wavelet Petrov–Galerkin solution is bounded by

$$|\varphi^\ell - \varphi|_{H^1([0,L])} \leq C \varrho^m \|\varphi\|_{H^{m+1}([0,L])} \tag{102}$$

*Proof.* Let

$$\begin{aligned} e &= \varphi^\ell - \varphi = w^\ell - w \\ &= (w^\ell - \mathcal{R}_\varrho^m w) + (\mathcal{R}_\varrho^m w - w) \equiv e^\ell + \eta \end{aligned} \tag{103}$$

where  $\varphi(x)$  is the exact solution of equation (63). Let

$$e^\varrho(x) = \sum_{I \in \Lambda} e_I^c \Psi_I^{[0]}(x) \quad (104)$$

$$\tilde{e}^\varrho(x) = \sum_{I \in \Lambda} e_I^c \Psi_I^{[1]}(x) \quad (105)$$

Define the local Peclet number  $p_e := |a|q/\kappa$ . By equation (96)

$$\begin{aligned} & \kappa \left( \frac{1}{2} Y(\tau) + p_e \tau (1 - C_B C_I) \right) \|e_{,x}^\varrho\|_{L^2([0,L])}^2 \\ & \leq B_{\text{WPG}}(e^\varrho; \tilde{e}^\varrho) \\ & = B_{\text{WPG}}(e - \eta; \tilde{e}^\varrho) \\ & \leq |B_{\text{WPG}}(\eta; \tilde{e}^\varrho)| \leftarrow B_{\text{WPG}}(e, \tilde{e}^\varrho) = 0 \\ & = |B(\eta, e^\varrho) + \tau \operatorname{sgn}(a) \int_0^L \tilde{e}^\varrho (-\kappa \eta_{,xx} + a \eta_{,x}) dx| \\ & \leq |B(\eta, e^\varrho)| + \tau |a|q |(\tilde{e}^\varrho/q, \eta_{,x})| + \tau \kappa q |(\tilde{e}^\varrho/q, \eta_{,xx})| \end{aligned} \quad (106)$$

By inequality (75),  $\exists \varepsilon_1, \varepsilon_2 > 0$  such that

$$\begin{aligned} B_{\text{WPG}}(e^\varrho; \tilde{e}^\varrho) & \leq |B(\eta, e^\varrho)| + \frac{\tau |a|q}{2} \left( \frac{1}{\varepsilon_1} \|\tilde{e}^\varrho/q\|_{L^2([0,L])}^2 + \varepsilon_1 \|\eta_{,x}\|_{L^2([0,L])}^2 \right) \\ & \quad + \frac{\tau \kappa q}{2} \left( \frac{1}{\varepsilon_2} \|\tilde{e}^\varrho/q\|_{L^2([0,L])}^2 + \varepsilon_2 \|\eta_{,xx}\|_{L^2([0,L])}^2 \right) \end{aligned} \quad (107)$$

Considering the triangular inequality, wavelet estimate (88), and inverse estimate (77), one has

$$\begin{aligned} \|\tilde{e}^\varrho/q\|_{L^2([0,L])}^2 & = \|\tilde{e}^\varrho/q - e_{,x}^\varrho + e_{,x}^\varrho\|_{L^2([0,L])}^2 \\ & \leq 2(\|\tilde{e}^\varrho/q - e_{,x}^\varrho\|_{L^2([0,L])}^2 + \|e_{,x}^\varrho\|_{L^2([0,L])}^2) \\ & \leq 2(C_B^2 C_I^2 + 1) \|e_{,x}^\varrho\|_{L^2([0,L])}^2 \end{aligned} \quad (108)$$

Following Hughes *et al.* [25], one may find that  $\exists \varepsilon > 0$  such that

$$|B(\eta, e^\varrho)| \leq \frac{\kappa}{2\varepsilon} \|e_{,x}^\varrho\|_{L^2([0,L])}^2 + \varepsilon \left( \frac{a^2}{\kappa} \|\eta\|_{L^2([0,L])}^2 + \kappa \|\eta_{,x}\|_{L^2([0,L])}^2 \right) \quad (109)$$

Then, dividing  $\kappa$  through (106), one has

$$\begin{aligned} & \left\{ \left( \frac{1}{2} Y(\tau) + \tau p_e (1 - C_B C_I) \right) \right\} \|e_{,x}^\varrho\|_{L^2([0,L])}^2 \\ & \leq \frac{1}{2\varepsilon} \|e_{,x}^\varrho\|_{L^2([0,L])}^2 + \frac{\varepsilon p_e^2}{q^2} \|\eta\|_{L^2([0,L])}^2 + \varepsilon \|\eta_{,x}\|_{L^2([0,L])}^2 \\ & \quad + \frac{\tau p_e}{2} \left( \frac{2}{\varepsilon_1} (C_B^2 C_I^2 + 1) \|e_{,x}^\varrho\|_{L^2([0,L])}^2 + \varepsilon_1 \|\eta_{,x}\|_{L^2([0,L])}^2 \right) \\ & \quad + \frac{\tau q}{2} \left( \frac{2}{\varepsilon_2} (C_B^2 C_I^2 + 1) \|e_{,x}^\varrho\|_{L^2([0,L])}^2 + \varepsilon_2 \|\eta_{,xx}\|_{L^2([0,L])}^2 \right) \end{aligned} \quad (110)$$

Find  $0 < \tau \leq \tau_1$ , such that (see Figure 20)

$$\frac{1}{2} Y(\tau) \geq \frac{1}{4} \quad (111)$$

Let  $Y(\tau) = \frac{1}{2}$ . We find

$$\tau_1 = C_B + \sqrt{C_B^2 + 0.5C_I^{-2}} \tag{112}$$

Substituting  $\tau_1$  back into (110) yields the following inequality:

$$\begin{aligned} & \left(\frac{1}{4} + p_e \tau_1 (1 - C_B C_I)\right) \|e_{,x}^e\|_{L^2([0,L])}^2 \\ & \leq \frac{1}{2\varepsilon} \|e_{,x}^e\|_{L^2([0,L])}^2 + \frac{\varepsilon p_e^2}{\varrho^2} \|\eta\|_{L^2([0,L])}^2 + \varepsilon \|\eta_{,x}\|_{L^2([0,L])}^2 \\ & \quad + \frac{p_e \tau_1}{2} \left( \frac{2}{\varepsilon_1} (C_B^2 C_I^2 + 1) \|e_{,x}^e\|_{L^2([0,L])}^2 + \varepsilon_1 \|\eta_{,x}\|_{L^2([0,L])}^2 \right) \\ & \quad + \frac{\varrho \tau_1}{2} \left( \frac{2}{\varepsilon_2} (C_B^2 C_I^2 + 1) \|e_{,x}^e\|_{L^2([0,L])}^2 + \varepsilon_2 \|\eta_{,xx}\|_{L^2([0,L])}^2 \right) \end{aligned} \tag{113}$$

Follow a similar procedure as in Hughes *et al.* [25] and let

$$\varepsilon = \frac{8}{(1 + p_e \tau_1 (1 - C_B C_I))} \tag{114}$$

$$\varepsilon_1 = \frac{4(C_B^2 C_I^2 + 1)}{3(1 - C_B C_I)} \tag{115}$$

$$\varepsilon_2 = \frac{16\varrho \tau_1 (C_B^2 C_I^2 + 1)}{(1 + p_e \tau_1 (1 - C_B C_I))} \tag{116}$$

We then arrive at the desired result

$$\begin{aligned} \|e_{,x}^e\|_{L^2([0,L])}^2 & \leq \frac{64 p_e^2}{\varrho^2 (1 + p_e \tau_1 (1 - C_B C_I))^2} \|\eta\|_{L^2([0,L])}^2 + \left\{ \frac{64}{(1 + p_e \tau_1 (1 - C_B C_I))^2} \right. \\ & \quad \left. + \frac{16(C_B^2 C_I^2 + 1) p_e \tau_1}{3(1 - C_B C_I)(1 + p_e \tau_1 (1 - C_B C_I))} \right\} \\ & \quad \times \|\eta_{,x}\|_{L^2([0,L])}^2 + \frac{64 \varrho^2 \tau_1^2 (C_B^2 C_I^2 + 1)}{(1 + p_e \tau_1 (1 - C_B C_I))} \|\eta_{,xx}\|_{L^2([0,L])}^2 \end{aligned} \tag{117}$$

To this end, it is clear that  $\exists C_0, C_1$ , and  $C_2 > 0$  such that

$$\begin{aligned} \|e^e\|_{H^1([0,L])}^2 & \leq C_0 \varrho^{-2} \|\eta\|_{L^2([0,L])}^2 + C_1 \|\eta_{,x}\|_{L^2([0,L])}^2 + C_2 \varrho^2 \|\eta_{,xx}\|_{L^2([0,L])}^2 \\ & \leq C_0 \varrho^{2m} \|w\|_{H^{m+1}([0,L])}^2 + C_1 \varrho^{2m} \|w\|_{H^{m+1}([0,L])}^2 + C_2 \varrho^{2m} \|w\|_{H^{m+1}([0,L])}^2 \\ & \leq \bar{C}^2 \varrho^{2m} \|w\|_{H^{m+1}([0,L])}^2 \end{aligned} \tag{118}$$

where constants  $C_0, C_1, C_2$  and  $\bar{C}$  are independent from  $p_e$ .

That is

$$\|e^e\|_{H^1([0,L])} \leq \bar{C} \varrho^m \|w\|_{H^{m+1}([0,L])} \tag{119}$$

Consequently,

$$\begin{aligned} |e|_{H^1([0,L])} & \leq |e^e|_{H^1([0,L])} + |\eta|_{H^1([0,L])} \\ & \leq \bar{C}_1 \varrho^m \|w\|_{H^{m+1}([0,L])} \end{aligned} \tag{120}$$

□

## 6. CONCLUDING REMARKS

The meshless hierarchical partition of unity developed in Part I of [1] has been applied to a number of practical engineering problems. It is shown that the wavelet hierarchical partition of unity developed in [1] enables us to perform some useful numerical operations, such as the wavelet adaptive refinement, or multiple scale computations. The multiple scale computation carried out here is beyond the so-called multiple scale analysis done by Liu *et al.* [3, 11, 17] and Liu and Chen. [2]. In those works, the multiple scale computation is achieved by varying the support size of the shape function, whereas in this paper the multiple scale computation is achieved by directly using the higher-order wavelet bases. The numerical results reported here indicate that the method is viable, and robust in the meshless environment. A wavelet Petrov–Galerkin method has proposed as a remedy in dealing with some pathological numerical computations, such as to avoid the volumetric ‘locking’ and convection dominated destabilization. A stability and convergence proof of the wavelet Petrov–Galerkin method is also presented for the one-dimensional advection–diffusion problem, which might provide few insight to the class of stabilization methods. In addition, there are some advantages of wavelet Petrov–Galerkin method over the conventional Petrov–Galerkin method; such as there is no need to employ discontinuous Galerkin approach, and there is no need to evaluate the higher order derivatives, which can save additional computations, especially in a meshless environment.

## ACKNOWLEDGEMENTS

The material presented in this paper is part of the first author’s (SL) Ph.D. dissertation [28] with some extension. This work is supported by grants from the Office of Naval Research, the Army Research Office, and National Science Foundations, and Tull Family Endowment Fund. The first author (SL) is also supported by Graham-Cabell fellowship from Northwestern University. This work is also sponsored in part by the Army High Performance Computing Research Center under the auspices of the Department of the Army, Army Research Laboratory cooperative agreement number DAAH04-95-2-003/contract number DAAH04-95-C-0008, the content of which does not necessarily reflect the position or the policy of the government, and no official endorsement should be inferred.

## REFERENCES

1. Li S, Liu WK. Reproducing kernel hierarchical partition of unity part 1: Formulation & theory. *International Journal for Numerical Methods in Engineering* 1999;**45**.
2. Liu WK, Chen Y. Wavelet and multiple scale reproducing kernel method. *International Journal of Numerical Methods in Fluids* 1995;**21**:901–933.
3. Liu WK, Chen Y, Chang CT, Belytschko T. Advances in multiple scale kernel particle methods. *Computational Mechanics* 1996;**18**:73–111.
4. Thompson LL, Pinsky P. A galerkin least-square finite element method for the two-dimensional helmholtz equation. *International Journal for Numerical Methods in Engineering* 1995;**38**:371–397.
5. Peirce D, Shih CF, Needleman A. A tangent modulus method for rate dependent solids. *Computers and Structures* 1984;**5**:875–887.
6. Ihlenburg F, Babuška I. Dispersion analysis and error estimation of galerkin finite element methods for the helmholtz equation. *International Journal for Numerical Methods in Engineering* 1995;**38**:3745–3774.
7. Duarte CA, Oden JT. *Hp* clouds—an *hp* meshless method. *Numerical Methods in Partial Differential Equations* 1996;**12**:673–705.
8. Ortiz M, Leroy Y, Needleman A. A finite element method for localized failure analysis. *Computer Methods in Applied Mechanics and Engineering* 1987;**61**:189–214.

9. Thompson LL, Pinsky P. Complex wavenumber fourier analysis of the  $p$ -version finite element method. *Computational Mechanics* 1994;**13**:255–275.
10. Needleman A. Dynamic shear band development in plane strain. *Journal of Applied Mechanics* 1989;**56**:1–9.
11. Liu WK, Jun S, Zhang S. Reproducing kernel particle methods. *International Journal of Numerical Methods in Fluids* 1995;**20**:1081–1106.
12. Needleman A. Material rate dependent and mesh sensitivity in localization problems. *Computer Methods in Applied Mechanics and Engineering* 1988;**67**:68–85.
13. Belytschko T, Chiang HY, Plaskacz E. High resolution two-dimensional shear band computations: imperfections and mesh dependence. *Computer Methods in Applied Mechanics and Engineering* 1994:1–15.
14. Belytschko T, Fish J, Bayliss A. The spectral overlay on finite elements for problems with high gradients. *Computer Methods in Applied Mechanics and Engineering* 1990;**81**:71–89.
15. Needleman A, Tvergaard V. Analysis of plastic flow localization in metals. *Applied Mechanics Review* 1992;**45**:S3–S18.
16. Hinton E, Rock T, Zienkiewicz OC. A note on mass lumping and related processes in finite element method. *Earthquake Engineering and Structural Dynamics* 1976;**4**:245–249.
17. Liu WK, Chen Y, Uras RA, Chang CT. Generalized multiple scale reproducing kernel particle methods. *Computer Methods in Applied Mechanics and Engineering* 1996;**139**:91–158.
18. Belytschko T, Tabbara M. H-adaptive finite element methods for dynamic problems with emphasis on localization. *International Journal for Numerical Methods in Engineering* 1993;**36**:4245–4265.
19. Johnson C, Nävert U, Pitärant J. Finite element methods for linear hyperbolic problems. *Computer Methods in Applied Mechanics and Engineering* 1984;**45**:285–312.
20. Johnson C, Szepessy A, Hansbo P. On the convergence of shock-capturing streamline diffusion finite element methods for hyperbolic conservation laws. *Mathematics Computation* 1990;**54**:107–129.
21. Franca LP, Hughes TJR. Convergence analysis of Galerkin-least-squares methods for symmetric advective–diffusive forms of the Stokes and incompressible Navier–Stokes equations. *Computer Methods in Applied Mechanics and Engineering* 1993;**105**:285–298.
22. Hughes TJR, Franca LP, Mallet M. A new finite element formulation for computational dynamics vi: Convergence analysis of the generalized supg formulation for linear time-dependent multidimensional advective–diffusive systems. *Computer Methods in Applied Mechanics and Engineering*, 1987;**63**:97–112.
23. Hughes TJR, Mallet M. A new finite element formulation for computational dynamics iii. the generalized streamline operator for multidimensional advective–diffusive systems. *Computer Methods in Applied Mechanics and Engineering* 1986;**58**:305–328.
24. Hughes TJR, Mallet M, Mizukami A. A new finite element formulation for computational dynamics ii. beyond supg. *Computer Methods in Applied Mechanics and Engineering* 1986;**54**:341–355.
25. Hughes TJR, Franca LP, Chalot F, Johan Z. Stabilized finite element methods in fluid mechanics. *Preprint*, Stanford University, 1994.
26. Gosz J, Liu WK. Admissible approximations for essential boundary conditions in the reproducing kernel particle method. *Computational Mechanics* 1996;**19**:120–135.
27. Brenner SC, Scott LR. *The Mathematical Theory of Finite Element Methods*; Springer: New York, 1994.
28. Li S. *Moving least square reproducing kernel methods*. PhD Thesis, McCormick School of Engineering and Applied Science, Northwestern University, Evanston, Illinois, May 1997.
29. Li S, Liu WK. Synchronized reproducing kernel interpolant via multiple wavelet expansion. *Computational Mechanics* 1998;**28**:28–47.
30. Tvergaard V, Needleman A, Lo KK. Flow localization in the plane strain tensile test. *Journal of Mechanics and Physics of Solids* 1981;**29**:115–142.
31. Uras RA, Chang CT, Liu WK. Multiresolution reproducing kernel particle methods in acoustics. *Journal of Computational Acoustics* 1997;**5**:71–94.
32. Hughes, TJR, Franca, LP, Balestra, M. A new finite element formulation for computational dynamics V: circumventing the Babuška–Brezzi condition: a stable Petrov–Galerkin formulation of the Stokes problem accommodating equal-order interpolations. *Computer Methods in Applied Mechanics and Engineering* 1986;**59**:85–99.